

Journal of Energy

ISSN 1849-0751 (On-line)
ISSN 0013-7448 (Print)
UDK 621.31
[https://doi.org/10.37798/
EN2025741](https://doi.org/10.37798/EN2025741)

VOLUME 74 Number 1 | 2025

- 03** Dubravko Sabolić, Igor Ivanković
Empirical Assessment of Wind Power's Capacity Credit: A European Case Study
- 09** Viktor Milardić, Amir Tokić, Anamari Nakić
Arc Flash Calculation for 110/20 kV HV/MV Substation
- 13** Mohammed Moyed Ahmed
Accurate Photovoltaic Power Forecasting in 5G Networks: A Novel Neural Network Approach
- 24** Mihael Boštjan Končar, Domen Hojkar, Boštjan Drobnič, Mihael Sekavčnik, Mitja Mori
Model-Based Comparison of Nuclear and Renewable Energy Based Strategies for Slovenia

Journal of Energy

Scientific Professional Journal Of Energy, Electricity, Power Systems

Online ISSN 1849-0751, Print ISSN 0013-7448, VOL 74

<https://doi.org/10.37798/EN2024741>

Published by

HEP d.d., Ulica grada Vukovara 37, HR-10000 Zagreb

HRO CIGRÉ, Berislavićeva 6, HR-10000 Zagreb

Publishing Board

Robert Krklec, (president) HEP, Croatia,

Goran Slipac, (vicepresident), HRO CIGRÉ, Croatia

Editor-in-Chief

Igor Kuzle, University of Zagreb, Croatia

Associate Editors

Murat Fahrioglu, Middle East Technical University, Cyprus

Tomislav Gelo, University of Zagreb, Croatia

Davor Grgić, University of Zagreb, Croatia

Marko Jurčević, University of Zagreb, Croatia

Marija Šiško Kuliš, HEP-Generation Ltd., Croatia

Goran Majstrovic, Energy Institute Hrvoje Požar, Croatia

Tomislav Plavšić, Croatian Transmission system Operator, Croatia

Goran Slipac, HRO CIGRÉ, Croatia

Matija Zidar, University of Zagreb, Croatia

International Editorial Council

Anastasios Bakirtzis, Aristotle University of Thessaloniki, Greece

Lina Bertling Tjernberg, KTH Royal Institute of Technology, Sweden

Tomislav Capuder, University of Zagreb, Croatia

Maja Muftić Dedović, University of Sarajevo, Bosnia and Herzegovina

Tomislav Dragičević, Technical University of Denmark, Denmark

Ante Elez, HEP Plc, Croatia

Dubravko Franković, University of Rijeka, Croatia

Hrvoje Glavaš, J. J. Strossmayer University of Osijek, Croatia

Božidar Filipović Grčić, University of Zagreb, Croatia

Josep M. Guerrero, Technical University of Catalonia, Spain

Juraj Havelka, University of Zagreb, Croatia

Dirk Van Hertem, KU Leuven, Belgium

Žarko Janić, Siemens-Končar-Power Transformers, Croatia

Chongqing Kang, Tsinghua University, China

Matej Krpan, Hitachi Energy Sweden AB, Sweden

Yongqian Liu, North China Electric Power University, China

Dražen Lončar, University of Zagreb, Croatia

Jovica Milanović, University of Manchester, UK

Viktor Milardić, University of Zagreb, Croatia

Damir Novosel, Quanta Technology, USA

Hrvoje Pandžić, University of Zagreb, Croatia

Ivan Pavić, University of Luxembourg, Luxembourg

Vivek Prakash, Banasthali Vidyapith, India

Ivan Rajšl, University of Zagreb, Croatia

Aleksandar M. Stankovic, Stanford University, USA

Luka V. Strezoski, University of Novi Sad, Serbia

Damir Sumina, University of Zagreb, Croatia

Zdenko Šimić, Paul Scherrer Institut, Switzerland

Vladimir Terzija, Newcastle University, UK

Bojan Trkulja, University of Zagreb, Croatia

István Vokony, Budapest University of Technology and Economics, Hungary

EDITORIAL

First article in this issue: “Empirical Assessment of Wind Power’s Capacity Credit: A European Case Study” examines the effective capacity credit of onshore wind power plants in selected European countries for the years 2019 and 2024. In addition to analyzing observed capacity credit in individual countries and across the continent, it explores hypothetical scenarios with alternative spatial distributions of wind capacity. Results show that optimized distributions yield higher intrinsic capacity credit compared to the actual configurations. This suggests that, under current electricity consumption profiles, coordinated allocation strategies could meaningfully improve the performance of wind generation.

The second paper “Arc Flash Calculation for 110/20 kV HV/MV Substation” presents an arc flash calculation for a 110/20 kV substation, based on the revised IEEE 1584:2018 standard, which replaces the 2002 version. The study focuses on medium-voltage switchgear compartments, with the highest risk identified in the connection compartments where the cable terminations are located. The results show that the incident energy is above the threshold of 1.2 cal/cm² and at least PPE Category 1 is required, while additional safety measures such as pressure relief ducts and arc-resistant designs may reduce the labelling requirements. The paper emphasises the importance of compliance with IEEE 1584:2018 and NFPA 70E:2024 standards, preventative maintenance, and appropriate training of personnel to mitigate arc flash hazards and ensure worker safety.

The article “Accurate Photovoltaic Power Forecasting in 5G Networks: A Novel Neural Network Approach” presents an Improved Firefly Algorithm-Back Propagation (IFA-BP) neural network for forecasting PV power in 5G base stations. By combining Circle chaos mapping and nonlinear perturbation, the model improves global search and convergence. The grey correlation analysis selects key inputs such as solar radiation, wind speed, and temperature. This hybrid approach avoids local minima and ensures reliable forecasts under varying weather. Experimental results show strong performance, with a MAPE of 4.79% (sunny) and 12.20% (cloudy), and an $R^2 > 0.97$. The model supports accurate, weather-adapted energy forecasting for sustainable 5G networks.

The article “Model-Based Comparison of Nuclear and Renewable Energy Based Strategies for Slovenia” provides a comprehensive analysis of Slovenia’s energy transition strategies, comparing nuclear and renewable energy-based approaches. Using a zero-dimensional energy system model, the study evaluates key metrics such as grid stability, carbon intensity, land use, and import/export dependency under two scenarios: one prioritizing nuclear power and the other focusing on renewables. The findings highlight nuclear power’s role in ensuring stable baseload generation, minimizing fluctuations, and reducing reliance on extensive storage or exports. In contrast, renewable-only strategies introduce significant variability, requiring costly balancing measures. The study underscores the importance of integrating nuclear energy into Slovenia’s decarbonization efforts while raising critical questions about the feasibility of renewable-only policies. This work offers valuable insights for policymakers and stakeholders navigating the complexities of sustainable energy planning.

Igor Kuzle
Editor-in-Chief

Empirical Assessment of Wind Power's Capacity Credit: A European Case Study

Dubravko Sabolić, Igor Ivanković

Summary — This paper presents an empirical analysis of the intrinsic capacity credit of onshore wind power across twelve European countries, based on hourly measured data for 2019 and 2024. Capacity credit was calculated as a function of acceptable default risk, under the simplifying assumption that wind power alone must satisfy total demand, serving as a limiting-case benchmark for adequacy assessment. The results show a wide range of outcomes across individual countries and highlight the effects of spatial aggregation, where the combined regional system performs better than its constituents. A nonlinear model was fitted to describe the relationship between capacity credit and risk probability. Additionally, several hypothetical spatial distributions of installed capacity were evaluated using statistical criteria, illustrating how coordination could affect adequacy outcomes. The analysis was based exclusively on observed data, without additional modeling assumptions, and the proposed method offers a transparent, generalizable framework for empirical adequacy benchmarking across generation types and planning contexts.

Keywords — Wind power, capacity credit, system adequacy, spatial distribution, empirical modeling

I. INTRODUCTION

Integration of renewable energy sources (RES) into modern power systems poses significant challenges related to system adequacy, short-term variability, and market integration. A variety of methodologies have been proposed to quantify the reliability contribution, or capacity credit, of wind and solar power.

Capacity credit, also known as capacity value, is defined as the contribution that a new generator makes to system adequacy without compromising overall reliability. In the context of RES investments, it reflects the share of system load that can be reliably met by new RES generation, accounting for its variability and alignment with system stress periods. It is typically expressed as a percentage. For example, if a wind plant has a capacity credit of 10%, only one-tenth of its installed capacity can be counted toward meeting the system's peak load with a high degree of reliability, typically around 99% to 99.9% of the time. This reliability depends on the criteria set by the TSO, often defined by the Loss of Load Expectation (LOLE) or Loss of Load Probability (LOLP) [1], [2].

Ensslin et al. [1] observe that onshore wind capacity credits in various systems ranged from as high as 40% of installed capacity in regions with low wind penetration and high capacity factors during peak load times to as low as 5% in regions with high wind penetration or low capacity factors. Jorgenson et al. [3] conducted a comprehensive evaluation of wind capacity credit across the Western United States using probabilistic reliability methods. Their findings show that the capacity credit of land-based wind varies significantly by region and weather year, ranging from 5% to 30%, and averages 16%. The study also demonstrates that capacity credit tends to increase with the capacity factor, but that correlation with times of system stress is an even more decisive factor—particularly for offshore wind, which shows substantially higher capacity credit due to better alignment with periods of high demand and system risk. Ssengonzi et al. [4] present an approach to estimating the capacity credit of RES, particularly wind and solar, as their penetration levels increase across regional power grids in the contiguous United States, concluding that the capacity credits for all RES technologies analyzed decrease with penetration rate, with 5% as a limiting order of magnitude at the regional level.

Relying solely on wind power without supporting technologies would require a significant degree of overbuilding to ensure system adequacy, due to its variability and limited firm capacity. In practice, the need for such excessive overbuilding can be significantly reduced even in a hypothetical fossil-free system through the integration of complementary assets such as flexible hydropower, energy storage systems, demand-side management, and potentially hydrogen-fired generation. These technologies can mitigate the effects of intermittency and improve the firm capacity contribution of wind, thus lowering the effective overbuild factor required to meet reliability targets.

The statistical properties of generation intermittency in a large wind power system in the USA, along with the resulting demand for regulation reserves, were thoroughly analyzed in [5] and later extended in [6] using a European dataset. Interestingly, both analyses identified the same statistical distribution governing short-term production variations, despite being based on data from fundamentally different systems and geographical contexts.

These statistical findings illustrate how physical characteristics of wind generation affect system-level reliability metrics, forming the foundation for capacity credit analysis.

(Corresponding author: Dubravko Sabolić)

Dubravko Sabolić and Igor Ivanković are with the Croatian Transmission System Operator (HOPS), Zagreb, Croatia (e-mails: dubravko.sabolic@hops.hr, igor.ivankovic@hops.hr)

II. THE DATA

The source of all data used in this study is the ENTSO-E Transparency Platform (<https://transparency.entsoe.eu/>). For this preliminary analysis, we selected hourly measured aggregate generation data from onshore wind power plants in twelve European countries, as well as the total hourly electricity consumption recorded in those same countries.

Table I lists the countries included in the study along with basic descriptive statistics for the wind power production time series utilized. Regarding the temporal dimension, two separate calendar years were selected for analysis: 2019. and 2024.

The intermediate years were intentionally omitted due to significant societal and market disruptions during that period. Specifically, 2020 and 2021 were marked by the COVID-19 pandemic and its well-known economic effects on electricity demand and industrial output. In its final quarter, 2021 also saw the onset of severe electricity price disruptions that ended over a decade of relative stability [7]. The situation further escalated in early 2022 with the onset of the war in Ukraine, leading to increased crisis levels and price volatility across energy markets. A gradual stabilization in both the energy sector and the broader economy followed throughout 2023. Including these atypical years would have confounded the baseline analysis aimed at comparability across relatively stable conditions. While we acknowledge the importance of learning from periods of disruption, our objective here is to provide a reference scenario based on operational norms. A broader temporal scope will be considered in future research.

As such, the years chosen for this study represent a relevant and balanced framing: 2019 as the last “normal” year before major disruptions, and 2024 as the first year of renewed market stability under the new circumstances.

In addition to basic descriptive statistics, we computed the pairwise coefficients of determination (R^2) between all wind power production vectors to assess the degree of linear correlation among the observed countries. These values reflect how well the variation in one country’s wind output can be linearly explained by another. The resulting matrix of R^2 values is shown in Table II. The upper triangle of the matrix contains R^2 values for the year 2019 (in green), and the lower triangle corresponds to 2024, making the table asymmetric. The color intensity increases with the magnitude of R^2 . It can be observed that moderately strong correlations in wind power production exist only in a few country pairs (indicated by more intense coloration and higher R^2 values), and that these correlations are consistently present in both analyzed years.

The following country codes are used throughout the analysis: AT – Austria, BG – Bulgaria, CRO – Croatia, CZ – Czech Republic, F – France, D+L – Germany and Luxembourg, GR – Greece, PL – Poland, PT – Portugal, RO – Romania, ES – Spain, and SUM – the aggregated total across all listed countries.

As of January 2024, the population (in millions) of these countries was: AT – 9.16, BG – 6.45, CRO – 3.86, CZ – 10.9, F – 48.6, D+L – 84.2, GR – 10.6, PL – 36.6, PT – 10.6, RO – 19.1, ES – 48.6; with a combined total of 278 million [8].

TABLE I
DESCRIPTIVE STATISTICS OF THE TIME SERIES USED IN THIS STUDY.

	P (GW)	S (%)	E (TWh)	E/P (TWh/GW)	CF (%)	Std. (GW)	Std./P (%)
2019							
Austria	3.035	3.36	7.97	2.63	29.98	0.82	27.11
Bulgaria	0.7	0.53	1.25	1.79	20.41	0.13	18.19
Croatia	0.616	0.62	1.46	2.37	27.07	0.14	23.31
Czech Republic	0.316	0.29	0.69	2.17	24.75	0.06	19.25
France	13.61	13.80	32.70	2.40	27.43	2.66	19.53
Germany+Lux.	52.946	42.26	100.17	1.89	21.60	8.77	16.57
Greece	2.355	2.44	5.79	2.46	28.07	0.46	19.45
Poland	5.808	6.14	14.57	2.51	28.63	1.23	21.14
Portugal	5.127	5.66	13.42	2.62	29.89	1.13	22.01
Romania	2.968	2.82	6.68	2.25	25.69	0.64	21.56
Spain	22.961	22.08	52.35	2.28	26.03	3.47	15.13
SUM	110.44	100	237.05	2.15	24.50	13.07	11.83
2024							
Austria	4.021	3.33	9.36	2.33	26.52	0.95	23.52
Bulgaria	0.705	0.48	1.35	1.91	21.81	0.14	19.78
Croatia	1.209	0.93	2.62	2.16	24.64	0.27	22.02
Czech Republic	0.342	0.25	0.69	2.03	23.17	0.06	17.66
France	22.134	14.84	41.79	1.89	21.56	3.63	16.42
Germany+Lux.	60.049	39.67	111.69	1.86	21.28	10.04	16.72
Greece	5.065	3.88	10.94	2.16	24.62	0.82	16.21
Poland	9.583	8.45	23.78	2.48	28.42	2.13	22.25
Portugal	5.333	4.99	14.04	2.63	29.99	1.16	21.72
Romania	2.958	2.25	6.33	2.14	24.38	0.65	21.82
Spain	30.159	20.94	58.94	1.95	22.26	3.87	12.84
SUM	141.56	100	281.52	1.99	22.71	16.54	11.68

Legend: P = Installed capacity. S = Share of installed capacity relative to the total for all displayed countries. E = Energy produced. CF = Capacity factor. Std. = Standard deviation.

TABLE II
MATRIX OF DETERMINATION COEFFICIENTS R^2 : 2019 (UPPER TRIANGLE, GREEN) AND 2024 (LOWER TRIANGLE, RED).

	AT	BG	CRO	CZ	F	D+L	GR	PL	PT	RO	ES
AT	1	0.010	0.046	0.346	0.024	0.060	0.001	0.102	0.008	0.037	0.020
BG	0.035	1	0.068	0.010	0.013	0.006	0.123	0.010	0.005	0.332	0.007
CRO	0.046	0.059	1	0.008	0.001	0.000	0.021	0.009	0.011	0.066	0.027
CZ	0.316	0.025	0.003	1	0.138	0.509	0.010	0.466	0.002	0.024	0.012
F	0.041	0.021	0.025	0.182	1	0.319	0.008	0.080	0.043	0.006	0.102
D+L	0.093	0.018	0.000	0.519	0.329	1	0.007	0.427	0.000	0.005	0.010
GR	0.010	0.140	0.017	0.002	0.001	0.000	1	0.001	0.000	0.020	0.000
PL	0.161	0.010	0.000	0.485	0.081	0.459	0.002	1	0.000	0.016	0.002
PT	0.023	0.002	0.021	0.026	0.099	0.022	0.000	0.011	1	0.006	0.545
RO	0.056	0.520	0.042	0.046	0.038	0.036	0.059	0.025	0.006	1	0.011
ES	0.038	0.012	0.073	0.036	0.196	0.034	0.001	0.013	0.434	0.025	1

III. METHODOLOGY

The primary objective of this study is to determine the effective capacity credit of onshore wind power plants in selected European countries over the analyzed years. To this end, hourly wind generation data were normalized with respect to the total installed capacity recorded at the end of each respective year. Similarly, the aggregate hourly wind generation for the entire group of twelve countries was normalized by the sum of installed capacities in all of them. While this simplification introduces some error — since installed capacity evolves over the year — the relative yearly growth is relatively small, and thus the approximation remains reasonable. The assumption of exclusive wind supply is not intended to reflect practical system planning but rather to define an upper-bound reference case that enables empirical comparison of adequacy outcomes across different spatial and temporal configurations. System load profiles, expressed as hourly electricity consumption, were normalized by the annual peak hourly demand. The intrinsic capacity credit — here referring strictly to onshore wind — was calculated using the following procedure: the time series of normalized wind generation was multiplied by a scalar factor F , and then the normalized system demand series was subtracted from the result. The percentage of hours r in which the resulting series was

negative was then determined. The capacity credit C , corresponding to a default risk of r , is defined as:

$$C = \frac{100}{F} \quad (1)$$

The empirically observed capacity credit values — interpretable as quantiles of a stochastic distribution at a given level of risk — were analyzed as a function of the default risk r . It was found that the relationship between C and r exhibits a high degree of correlation with the inverse distribution function of short-term production fluctuations, as previously established in our earlier works [5], [6].

Specifically, we find that the capacity credit can be very accurately modeled as a composite function of the form:

$$C(r) = a \cdot r^b + c \cdot r + \varepsilon \quad (2)$$

where a , b , and c are empirically fitted parameters, and ε is the residual error term capturing the difference between the observed and modeled values of capacity credit. Both $C(r)$ and r are expressed as percentages. Despite its nonlinearity, the model remains interpretable and tractable for practical use. In addition to directly analyzing the observed capacity credit in individual countries and across the entire contiguous geographic region — spanning the full width of the European continent — this study also investigates hypothetical scenarios in which the spatial distribution of installed wind capacity differs from the actual configuration. These scenarios preserve the measured temporal characteristics of normalized production and consumption while varying the relative distribution of installed capacity.

Several alternative spatial configurations were developed, each optimized to improve general indicators of variability—such as minimizing the overall variance of wind generation or maximizing the ratio of total production to its variability. These simulations illustrate the potential benefits of a more coordinated approach to the geographic allocation of wind capacity. The findings indicate that such hypothetical redistribution strategies could yield a higher intrinsic capacity credit compared to the currently observed configuration. However, as the analysis is based on time series from only two individual years, the conclusions remain indicative rather than definitive, highlighting the need for broader temporal coverage in future research.

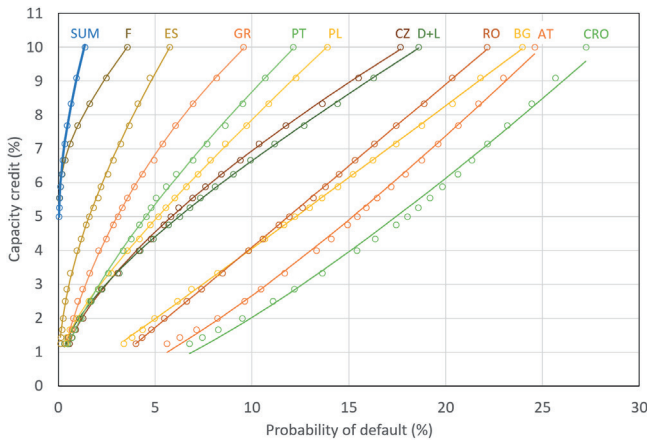


Fig. 1. Capacity credit vs. default probability for 2019.

It is important to emphasize that the intrinsic capacity credit analyzed above was derived through direct empirical observation — essentially “watching nature” — based on measured onshore wind production and total electricity consumption. As such, it inherently captures the full spectrum of stochastic events that occurred during the two years studied, including unpredictable production and demand fluctuations, forced outages, plant shutdowns, localized demand drops, and similar disturbances, which makes it highly relevant within the temporal and geographical scope of the analysis.

Evidently, this type of analysis can be easily extended to include any combination of generation technologies, in any real or simulated configuration, provided that comparable temporal and operational data are available.

IV. THE RESULTS

A. ACTUAL SPATIAL DISTRIBUTION ACROSS THE COUNTRIES

Figure 1 shows the relationship between capacity credit and the probability of failing to meet instantaneous demand for the year 2019. The dots represent empirically determined values, while the lines correspond to the best-fit regression curves based on (2), obtained by minimizing the total squared error. Figure 2 presents the same type of analysis for the year 2024. Table III summarizes the

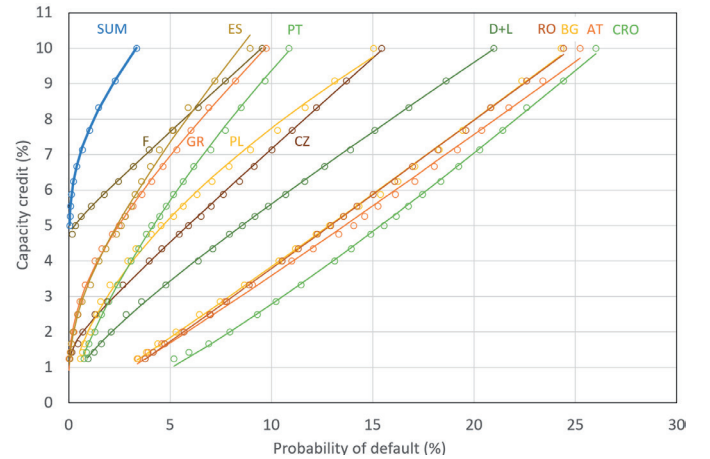


Fig. 2. Capacity credit vs. default probability for 2024.

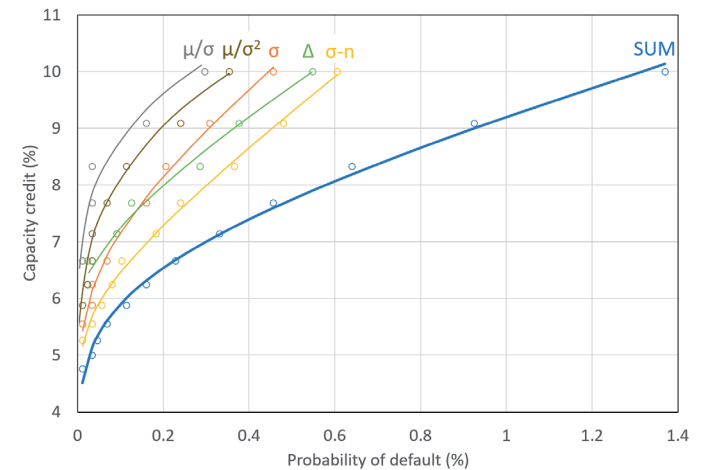


Fig. 3. Capacity credit vs. default probability under multiple hypothetical optimized spatial distributions for 2019.

TABLE III

FITTED REGRESSION PARAMETERS AND R^2 COEFFICIENTS FOR EACH COUNTRY AND YEAR.

		a	b	c	R^2
2019	Austria	-2.935	1.062	2.830	0.9979
	Bulgaria	-2.560	1.005	2.938	0.9996
	Croatia	-2.878	1.066	2.698	0.9936
	Czech Republic	1.650	1.868	0.128	0.9995
	France	7.065	12.128	0.606	0.9996
	Germany+Lux.	1.677	2.611	0.260	0.9997
	Greece	4.013	1.213	-1.657	0.9991
	Poland	1.556	3.150	0.463	0.9998
	Portugal	1.608	1.642	0.215	0.9991
	Romania	-0.595	8.852	0.487	0.9998
	Spain	3.502	2.347	0.455	0.9976
	SUM	7.808	7.359	1.403	0.9985
2024	Austria	-1.720	1.018	2.010	0.9976
	Bulgaria	-0.905	1.027	1.235	0.9989
	Croatia	-1.150	1.154	1.124	0.9991
	Czech Republic	1.730	8.824	0.491	0.9995
	France	4.960	61.013	0.510	0.9992
	Germany+Lux.	0.991	2.826	0.337	0.9997
	Greece	3.060	3.724	0.451	0.9981
	Poland	2.094	1.717	-0.026	0.9964
	Portugal	2.738	1.166	-1.035	0.9994
	Romania	-0.271	3.696	0.429	0.9995
	Spain	2.862	3.401	0.551	0.9955
	SUM	7.134	9.552	0.573	0.9989

Legend: Regression: $C(r) = a r^b + c r + \varepsilon$. The probability of default (r) and the capacity credit (C) are expressed as percentages (%). R^2 is the determination coefficient.

fitted regression coefficients and their corresponding R^2 values for each case. Residual errors between modeled and observed capacity credit values were generally small — typically below 1.5 percentage points — confirming a close fit between the nonlinear model and the empirical data.

In both analyzed years, two distinct groups of countries can be observed: RO, BG, AT, and CRO on one side, and the remaining countries on the other. The four mentioned countries, at least within the years considered, exhibit insufficient intrinsic capacity credit from wind generation — meaning that reasonable values of capacity credit, on the order of 5 to 10 percent, only occur under relatively unfavorable default risk thresholds. In other words, relying on wind generation as the only renewable generation technology in them would be very costly in terms of additional resources, such as storage facilities, network upgrades, etc., needed to ensure system adequacy and stabilize the grid.

It is also worth noting that in both years, the SUM curve exhibited the most favorable trade-off between probability of default and capacity credit. Specifically, a 10% capacity credit level was attainable with a default probability of just 2–3%, which, while higher than typical reliability targets used by system operators, provides a useful reference point for comparing adequacy outcomes across configurations.

Given the limited scope of this study, these preliminary findings should be revisited and verified using a considerably broader dataset.

B. HYPOTHETICAL GEOGRAPHIC ALLOCATIONS YIELDING GREATER CAPACITY CREDIT

This naturally raises the question of whether, through hypothetical policies involving quotas for the installation of wind power (or other types of renewable energy), it would be possible — now or in the future—to achieve a higher overall level of system adequacy, that is, a higher capacity credit for the same level of supply risk.

To investigate this, we used the normalized time series of wind generation from all participating countries and determined the optimal relative distribution of installed capacity based on several criteria. These included: minimizing the standard deviation of total production (denoted σ); minimizing the standard deviation of net production — defined as total generation minus load — (denoted σ_n); minimizing the maximum absolute hourly change in total production (denoted Δ); maximizing the ratio between total annual energy production and the standard deviation (denoted μ/σ); and maximizing the ratio between total annual energy production and the variance (denoted μ/σ^2). These symbols are used to distinguish the respective scenarios in Figures 3 and 4.

In all scenarios, the optimized spatial distributions yielded better outcomes than the actual installed capacity distribution. This suggests that, at least in principle and under current electricity consumption profiles, the implementation of coordinated allocation policies could lead to a meaningful improvement in the overall intrinsic capacity credit of this generation technology.

On the other hand, we must emphasize that coordinating such policies at a multinational level across this scale would likely prove extremely challenging, if not infeasible.

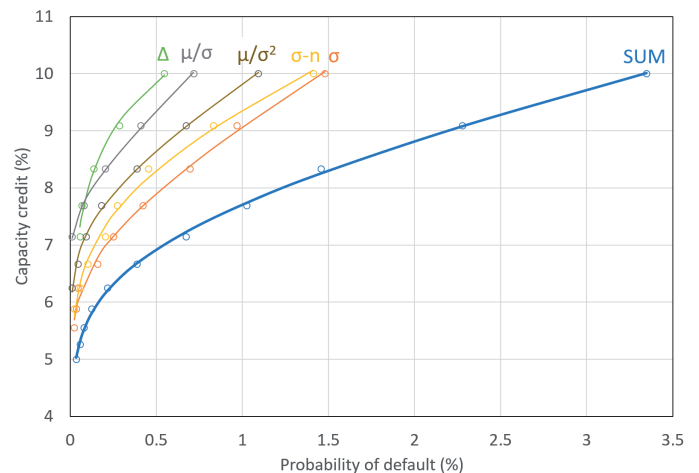


Fig. 4. Capacity credit vs. default probability under multiple hypothetical optimized spatial distributions for 2024.

TABLE IV

OPTIMAL HYPOTHETICAL VS. OBSERVED SPATIAL DISTRIBUTIONS OF INSTALLED CAPACITY ACROSS COUNTRIES, BASED ON SELECTED OPTIMIZATION CRITERIA.

Scenario	2019			2024		
	Actual	Δ	μ/σ	Actual	Δ	μ/σ
Austria	3.363	5.195	4.364	3.326	1.146	1.903
Bulgaria	0.528	8.575	0	0.479	9.807	0
Croatia	0.616	17.80	6.635	0.929	12.10	8.140
Czech Republic	0.289	3.121	0	0.246	2.668	1.628
France	13.80	13.89	10.40	14.84	7.185	2.196
Germany+Lux.	42.26	0.695	7.864	39.67	8.302	8.196
Greece	2.442	8.359	24.33	3.885	3.814	28.99
Poland	6.145	8.653	11.20	8.446	6.949	9.874
Portugal	5.663	15.65	6.239	4.987	14.38	8.026
Romania	2.818	1.810	7.833	2.248	5.291	4.316
Spain	22.08	16.25	21.14	20.94	28.35	26.74

Legend: Δ – optimized by the first-order difference; μ/σ – optimized by the ratio of the mean to the standard deviation. All values are expressed as percentages (%).

Figures 3 and 4 illustrate the relationship between capacity credit and default probability under the optimized spatial distributions for 2019 and 2024, respectively. Each curve represents one of the optimization scenarios introduced earlier. In all cases, the curves lie to the left of the reference curve for the actual spatial distribution (SUM), confirming that improved adequacy outcomes can, in principle, be achieved through optimized geographic allocation.

Table IV provides a comparative overview of the optimal relative distribution of installed capacity by country for both analyzed years, along with a comparison to the observed (actual) distribution. For the sake of brevity, the table includes only the results of optimizations according to two specific criteria: the minimum peak absolute hourly change in total production (denoted by the symbol Δ) and the ratio of total annual production to its standard deviation (denoted as μ/σ). These results should be interpreted in the context of each country's relative size. Population, as referenced in Section II, serves as a reasonable proxy for national scale, though additional factors—such as the land area available for specific types of power generation—may also be relevant.

For example, in the case of Croatia — which, apart from Luxembourg, is the smallest of the countries included — it would be practically impossible to allocate 17.80% of the total wind capacity, as suggested by the optimization result under the Δ scenario in Table IV for the year 2019. Since the total installed capacity across all countries now exceeds 140 GW, such a share would imply more than 25 GW of wind power within Croatia alone, which is unrealistic given the country's limited territorial area.

Consequently, more advanced future research should incorporate upper bounds on installable capacity per country into the optimization problem, taking into account territorial, regulatory, and political constraints. Other system-level limitations, such as the impact of high wind penetration on reduced system inertia and frequency stability, may also play a role and merit further consideration in future studies.

V. DISCUSSION AND FUTURE WORK

The analysis presented in this paper provides a preliminary empirical view of the intrinsic capacity credit of wind power across twelve European countries, highlighting several aspects that may warrant further investigation.

One limitation of the study is the relatively narrow temporal

scope, covering only the years 2019 and 2024. These years were deliberately selected to represent conditions before and after a period of significant systemic disruptions. However, expanding the time horizon could help assess the robustness of the observed patterns and improve generalizability. On the other hand, the geographic scope of the study, which includes a diverse cross-section of southern, central, and southeastern Europe with a combined population of 278 million, may provide a representative basis for regional system-level considerations, although it can be broadened, too.

A perhaps noteworthy observation is the similarity in functional form between the dependence of capacity credit on default probability and that of the so-called regulation multiplier—a proxy for the demand for secondary regulation reserves—on default probability, as identified in our earlier studies [5], [6]. Although the variables involved are not the same, and the underlying mechanisms differ, the resemblance in empirical structure invites further examination. At present, the reason for this alignment remains unclear.

Another aspect observed in both analyzed years is that the aggregated capacity credit across all countries consistently exceeded the values obtained for any individual country. This is broadly consistent with the idea that geographic diversification helps mitigate the variability of renewable generation and supports system adequacy.

Results from the hypothetical spatial allocation scenarios suggest that an alternative geographic distribution of installed capacity could lead to improved adequacy outcomes. Although the methodology shows what could, in principle, be achieved, it is unlikely that such optimizations could be implemented in practice. Wind power deployment is largely driven by decentralized and private investment decisions, and coordinated planning across national boundaries poses considerable institutional and political challenges.

One strength of this approach is that it relies solely on measured data. As such, the observed outcomes reflect the actual variability and characteristics of the power system during the period in question, including both planned and unplanned events. Within the limits of data resolution, accuracy, and scope, the method captures realistic conditions without additional modeling assumptions.

Furthermore, the same approach could be extended to other types of generation, or to study marginal effects when additional capacity is introduced or removed from an existing system. These directions may be useful for future research, particularly in the context of mixed technology portfolios or systems undergoing transitions toward higher shares of renewable energy.

VI. CONCLUSIONS

This study explored the intrinsic capacity credit of wind power across a set of twelve European countries, based on measured hourly data for the years 2019 and 2024. The analysis was conducted under the assumption that wind generation would be the sole source of supply, allowing for a direct assessment of how reliably it could meet demand without additional system support.

The results showed significant variation in capacity credit values among countries, with consistently higher values obtained when production was aggregated across the entire region. This is consistent with the notion that spatial diversification can help mitigate the intermittency of wind generation.

A nonlinear regression model was fitted to describe the relationship between capacity credit and default probability. While the model provided a good empirical fit, its similarity to previously observed structures in reserve-related studies remains unexplained and may be a subject of future investigation.

Additionally, hypothetical spatial redistributions of installed capacity were evaluated using several statistical optimization criteria. These scenarios produced improved adequacy outcomes compared to the actual capacity distribution, although their practical implementation would likely face considerable challenges.

This provides a foundation for potential extensions, such as analyzing mixed technology portfolios or assessing marginal contributions of additional capacity under different system configurations.

REFERENCES

- [1] C. Ensslin, M. Milligan, H. Holttinen, M. O'Malley, and A. Keane, "Current Methods to Calculate Capacity Credit of Wind Power, IEA Collaboration," in 2008 IEEE Power and Energy Society General Meeting. IEEE, 2008. [Online]. Available: <https://www.researchgate.net/publication/4361034>
- [2] A. Keane, M. R. Milligan, C. Dent, B. Hasche, C. D'Annunzio, K. Dragoon, H. Holttinen, N. Samaan, L. Söder, and M. O'Malley, "Capacity Value of Wind Power," IEEE Transactions on Power Systems, vol. 26, no. 2, pp. 564–572, 2011. [Online]. Available: <https://www.researchgate.net/publication/224173319> Capacity value of wind power IEEE Trans Power Syst
- [3] J. Jorgenson, S. Awara, G. Stephen, and T. Mai, "A Systematic Evaluation of Wind's Capacity Credit in the Western United States," Wind Energy, vol. 24, pp. 1107–1121, 2021. [Online]. Available: <https://doi.org/10.1002/we.2620>
- [4] J. Ssengonzi, J. X. Johnson, and J. F. DeCarolis, "An Efficient Method to Estimate Renewable Energy Capacity Credit at Increasing Regional Grid Penetration Levels," Renewable and Sustainable Energy Transition, vol. 2, p. 100033, 2022. [Online]. Available: <https://doi.org/10.1016/j.rset.2022.100033>
- [5] D. Sabolić, "Statistical Properties of Wind Generation Time Series in the Pacific Northwest Region of the USA," Journal of Sustainable Development of Energy, Water and Environment Systems, vol. 5, no. 3, pp. 447–465, 2017. [Online]. Available: <http://dx.doi.org/10.13044/j.sdewes.d5.0156>
- [6] D. Sabolić, I. Ivanković, A. Andrić, and A. Župan, "On Short-term Variations of RES Power Generation and Associated Secondary Regulation Demand," in Innovative Smart Grid Technologies Europe (ISGT EUROPE), IEEE. IEEE, 2024. [Online]. Available: <https://ieeexplore.ieee.org/document/10863761>
- [7] ACER, "High energy prices," EU Agency for the Cooperation of Energy Regulators, Tech. Rep., October 2021. [Online]. Available: <https://energy.ec.europa.eu/document/download/6fb3259a-d738-4138-9ce8-cl1bfc2fb5dc/en?prefLang=hu>
- [8] Eurostat, "Population on 1 January by age and sex," <https://ec.europa.eu/eurostat/databrowser/view/tps00001/default/table?lang=en>, 2024, accessed April 2025.

Arc Flash Calculation for 110/20 kV HV/MV Substation

Viktor Milardić, Amir Tokić, Anamari Nakić

Summary — This paper presents arc flash calculation for 110/20 kV HV/MV substation that follows IEEE 1584:2018 Standard. The IEEE 1584:2018 standard has been completely revised compared to the IEEE 1584:2002 standard, and according to the IEEE 1584:2002 standard, the calculation of an electric arc can no longer be performed. The paper shows how calculating the risk assessment to identify potential electrical hazards and implement appropriate safety measures and ultimately to protect workers from arc-flash hazards. Arc flash calculation for the case of real 110/20 kV substation is shown.

Keywords — Calculation, Arc flash, IEEE 1584:2018 Standard.

I. INTRODUCTION

An arc flash is a dangerous electrical explosion caused by an arc fault, which occurs when electrical current leaves its intended path and travels through the air between conductors or from a conductor to ground. This can happen due to various reasons, such as equipment failure, improper installation, or maintenance errors. Arc flashes can be triggered by factors like dust, corrosion, condensation, or accidental contact with live parts.

The explosion can reach temperatures up to 20 000 °C, causing severe burns, hearing loss, and even fatalities. It can also vaporize metal parts and create a pressure wave that can damage equipment and injure personnel.

Implementing proper safety measures, such as regular maintenance, using arc-resistant switchgear, and ensuring proper training and use of personal protective equipment, can significantly reduce the risk.

Compliance with standards IEEE 1584: 2018 [1] [2], NFPA 70E: 2024 [3] and paper [4] is crucial for ensuring safety and minimizing arc flash hazards.

II. BASIC OF IEEE STANDARD 1584

IEEE 1584 Standard helps protect workers from arc-flash hazards. The standard provides mathematical models to calculate the arc-flash hazard distance and the incident energy to which workers could be exposed during their work on or near electrical equipment.

In relation to IEEE 1584:2002 standard, the IEEE 1584:2018 standard has been completely changed, and according to the IEEE 1584:2002 standard, arc flash calculation can no longer be performed.

For more details, see the changes in the document IEEE 1584_2018-2002_redline.

It defines the amount of thermal energy impressed on a surface at a certain distance from the source of an arc flash. This helps in determining the appropriate level of personal protective equipment (PPE) required.

IEEE 1584 Standard includes equations to calculate the arcing fault current, which is essential for understanding the potential severity of an arc flash.

The standard considers different electrode configurations and enclosure sizes, which significantly impact the arc-flash hazard calculations.

The latest version, IEEE 1584-2018, includes new equations and guidance for more accurate arc-flash hazard assessments, reflecting extensive testing and model development.

NFPA 70E, Standard for Electrical Safety in the Workplace, is a critical standard to ensure electrical safety for employees in the workplace.

NFPA 70E defines approach boundaries to protect workers from electrical hazards. These boundaries establish safe working distances around energized electrical conductors or circuit parts.

The standard requires a thorough risk assessment to identify potential electrical hazards and implement appropriate safety measures. This includes evaluating the likelihood of an arc flash and its potential severity.

NFPA 70E specifies the types of PPE required for different levels of electrical exposure. This includes flame-resistant clothing, gloves, face shields, and other protective gear. Employees must be trained in safe work practices and emergency procedures. The standard emphasizes the importance of regular training and drills to ensure workers are prepared for potential electrical incidents.

IEEE 1584 provides empirical formulas for determining arcing fault currents, incident energy and arc-flash boundary. This Standard establishes a ten-step procedure for gathering data and calculating arc flash hazard as follows:

- Collect the system and installation data
- Determine the system modes of operation
- Determine the bolted fault currents
- Determine typical gap and enclosure size based upon system voltages and classes of equipment
- Determine the equipment electrode configuration
- Determine the working distances

(Corresponding author: Viktor Milardić)

Viktor Milardić and Anamari Nakić are with the University of Zagreb Faculty of electrical engineering and computing, Zagreb, Croatia (e-mails: viktor.milardic@fer.hr, anamari.nakic@fer.hr)

Amir Tokić is with the Faculty of Electrical Engineering, University of Tuzla, Tuzla, Bosnia and Herzegovina (e-mail: amir.tokic@untz.ba)

- Calculation of arcing current
- Determine the arc duration
- Calculate the incident energy
- Determine the arc-flash boundary for all equipment

In the next part of the text, simplified calculation procedures for calculation of the arc currents, incident energy and arc-flash boundary are presented.

(1) The intermediate average arcing currents can be determined using the relation:

$$I_{arc_Voc} = 10^{k_1+k_2\log I_{bf}+k_3\log G} \sum_{i=4}^{10} k_i I_{bf}^{10-i} \quad (1)$$

where are:

I_{bf} - the bolted fault current for three-phase faults (symmetrical rms) [kA]

I_{arc_Voc} - the average rms arcing current at $V_{oc} = 600$ V [kA]

I_{arc_Voc} - the average rms arcing current at $V_{oc} = 2700$ V [kA]

I_{arc_Voc} - the average rms arcing current at $V_{oc} = 14\,300$ V [kA]

G - the gap distance between electrodes [mm]

k_1, \dots, k_{10} - the coefficients regard to [1]

(2) The reduced arcing currents, including the variation correction factor, are calculated from relations:

$$VarC_f = \sum_{i=1}^7 k_i V_{oc}^{7-i} \quad (2)$$

$$I_{arc_min} = I_{arc} (1 - 0.5 VarC_f) \quad (3)$$

where are:

$VarC_f$ - the arcing current variation correction factor

I_{arc} - the final or intermediate rms arcing current(s) [kA]

I_{arc_min} - the second rms arcing current reduced based on the variation correction factor [kA]

V_{oc} - the open-circuit voltage between 0.208 and 15.0 (20.0) [kV]

k_1, \dots, k_7 - the coefficients regard to [1]

(3) The final arcing current can be determined using the next equations:

$$I_{arc_1} = \frac{I_{arc_2700} - I_{arc_600}}{2.1} (V_{oc} - 2.7) + I_{arc_2700} \quad (4)$$

$$I_{arc_2} = \frac{I_{arc_14300} - I_{arc_2700}}{11.6} (V_{oc} - 14.3) + I_{arc_14300} \quad (5)$$

$$I_{arc_3} = \frac{I_{arc_1}}{2.1} (2.7 - V_{oc}) + \frac{I_{arc_2}}{2.1} (V_{oc} - 0.6) \quad (6)$$

where are:

I_{arc_1} - the first I_{arc} interpolation term between 600 V and 2700 V [kA]

I_{arc_2} - the second I_{arc} interpolation term used when V_{oc} is greater than 2700 V [kA]

I_{arc_3} - the third I_{arc} interpolation term used when V_{oc} is less than 2700 V [kA]

V_{oc} - the open-circuit voltage (system voltage) [kV]

(4.a) The equivalent height and width are determined using the next relations:

$$Width_1 = \frac{1}{25.4} \left(660.4 + (Width - 660.4) \frac{V_{oc}+A}{B} \right) \quad (7)$$

$$Height_1 = \frac{1}{25.4} \left(660.4 + (Height - 660.4) \frac{V_{oc}+A}{B} \right) \quad (8)$$

where are:

$Width_1$ - the equivalent enclosure width

$Height_1$ - the equivalent enclosure height

$Width$ - the actual enclosure width [mm]

$Height$ - the actual enclosure height [mm]

V_{oc} - the open-circuit voltage (system voltage) [kV]

A - constant equal to 4 for VCB and 10 for VCBB and HCB

B - constant equal to 20 for VCB, 24 for VCBB and 22 for HCB

The following electrode configurations (test arrangements) are defined.

VCB: Vertical conductors/electrodes inside a metal box/enclosure

VCBB: Vertical conductors/electrodes terminated in an insulating barrier inside a metal box/enclosure

HCB: Horizontal conductors/electrodes inside a metal box/enclosure

VOA: Vertical conductors/electrodes in open air

HOA: Horizontal conductors/electrodes in open air.

The general guidelines to determine the equivalent enclosure height and width for different ranges of enclosure dimensions and electrode configurations are presented in [1].

(4.b) The equivalent enclosure size (EES) is determined using the equivalent width and height from relation:

$$EES = \frac{Height_1 + Width_1}{2} \quad (9)$$

where are:

$Width_1$ - the equivalent enclosure width

$Height_1$ - the equivalent enclosure height

EES - the equivalent enclosure size

(4.c) The correction factor (CF) for a "Typical Enclosure" is obtained by using relation:

$$CF = b_1 EES^2 + b_2 EES + b_3 \quad (10)$$

The correction factor (CF) for a "Shallow Enclosure" is obtained by using relation:

$$CF = \frac{1}{b_1 EES^2 + b_2 EES + b_3} \quad (11)$$

where are:

b_1, b_2, b_3 - the coefficients refer to [1]

CF - the enclosure size correction factor

EES - the equivalent enclosure size (for typical box enclosures the minimum value of EES is 20)

(5) The intermediate incident energy values are calculated using the next relations:

$$E_{600} = \frac{12.552}{50} T \cdot 10^{k_1+k_2\log G + \frac{k_3 I_{arc_600}}{\sum_{i=4}^{10} k_i I_{bf}^{11-i}} + k_{11}\log I_{bf} + k_{12}\log D + k_{13}\log I_{arc_600} + \log \frac{1}{CF}} \quad (12)$$

$$E_{2700} = \frac{12.552}{50} T \cdot$$

$$10^{k_1+k_2 \log G + \frac{k_3 I_{\text{arc}_2700}}{\sum_{i=4}^{10} k_i I_{\text{bf}}^{11-i}} + k_{11} \log I_{\text{bf}} + k_{12} \log D + k_{13} \log I_{\text{arc}_2700} + \log \frac{1}{CF}} \quad (13)$$

$$E_{14300} = \frac{12.552}{50} T \cdot$$

$$10^{k_1+k_2 \log G + \frac{k_3 I_{\text{arc}_14300}}{\sum_{i=4}^{10} k_i I_{\text{bf}}^{11-i}} + k_{11} \log I_{\text{bf}} + k_{12} \log D + k_{13} \log I_{\text{arc}_14300} + \log \frac{1}{CF}} \quad (14)$$

where are:

E_{600} - the incident energy at $V_{\text{oc}} = 600 \text{ V}$ [J/cm^2]

E_{2700} - the incident energy at $V_{\text{oc}} = 2700 \text{ V}$ [J/cm^2]

E_{14300} - the incident energy at $V_{\text{oc}} = 14\,300 \text{ V}$ [J/cm^2]

T - the arc duration [ms]

G - the gap distance between conductors (electrodes) [mm]

I_{arc_600} - the rms arcing current for 600 V [kA]

I_{arc_2700} - the rms arcing current for 2700 V [kA]

I_{arc_14300} - the rms arcing current for $14\,300 \text{ V}$ [kA]

I_{bf} - the bolted fault current for three-phase faults

(symmetrical rms) [kA]

D - the distance between electrodes and calorimeters (working distance) [mm]

CF - the correction factor for enclosure size ($CF = 1$ for VOA and HOA configurations)

k_1, \dots, k_{13} - the coefficients regard to [1]

(6) The final incident energy values are estimated using the next equations:

$$E_1 = \frac{E_{2700} - E_{600}}{2.1} (V_{\text{oc}} - 2.7) + E_{2700} \quad (15)$$

$$E_2 = \frac{E_{14300} - E_{2700}}{11.6} (V_{\text{oc}} - 14.3) + E_{14300} \quad (16)$$

$$E_3 = \frac{E_1}{2.1} (2.7 - V_{\text{oc}}) + \frac{E_2}{2.1} (V_{\text{oc}} - 0.6) \quad (17)$$

where are:

E_1 - the first E interpolation term between 600 V and 2700 V [J/cm^2]

E_2 - the second E interpolation term used when V_{oc} is greater than 2700 V [J/cm^2]

E_3 - the third E interpolation term used when V_{oc} is less than 2700 V [J/cm^2]

V_{oc} - the open-circuit voltage (system voltage) [kV]

(7) The intermediate arc-flash boundary values are calculated using the next relations:

$$AFB_{600} = \frac{10^{k_1+k_2 \log G + \frac{k_3 I_{\text{arc}_600}}{\sum_{i=4}^{10} k_i I_{\text{bf}}^{11-i}} + k_{11} \log I_{\text{bf}} + k_{13} \log I_{\text{arc}_600} + \log \frac{1}{CF} - \log \frac{20}{T}}}{-k_{12}} \quad (18)$$

$$AFB_{2700} = \frac{10^{k_1+k_2 \log G + \frac{k_3 I_{\text{arc}_2700}}{\sum_{i=4}^{10} k_i I_{\text{bf}}^{11-i}} + k_{11} \log I_{\text{bf}} + k_{13} \log I_{\text{arc}_2700} + \log \frac{1}{CF} - \log \frac{20}{T}}}{-k_{12}} \quad (19)$$

$$AFB_{14300} = \frac{10^{k_1+k_2 \log G + \frac{k_3 I_{\text{arc}_14300}}{\sum_{i=4}^{10} k_i I_{\text{bf}}^{11-i}} + k_{11} \log I_{\text{bf}} + k_{13} \log I_{\text{arc}_14300} + \log \frac{1}{CF} - \log \frac{20}{T}}}{-k_{12}} \quad (20)$$

where are:

AFB_{600} - the arc-flash boundary for $V_{\text{oc}} = 600 \text{ V}$ [mm]

AFB_{2700} - the arc-flash boundary for $V_{\text{oc}} = 2700 \text{ V}$ [mm]

AFB_{14300} - the arc-flash boundary for $V_{\text{oc}} = 14\,300 \text{ V}$ [mm]

T - the arc duration [ms]

G - the gap distance between conductors (electrodes) [mm]

I_{arc_600} - the rms arcing current for 600 V [kA]

I_{arc_2700} - the rms arcing current for 2700 V [kA]

I_{arc_14300} - the rms arcing current for $14\,300 \text{ V}$ [kA]

I_{bf} - the bolted fault current for three-phase faults

(symmetrical rms) [kA]

D - the distance between electrodes and calorimeters (working distance) [mm]

CF - the correction factor for enclosure size ($CF = 1$ for VOA and HOA configurations)

k_1, \dots, k_{13} - the coefficients regard to [1]

(8) The final arc-flash boundary values are calculated using the next relations:

$$AFB_1 = \frac{AFB_{2700} - AFB_{600}}{2.1} (V_{\text{oc}} - 2.7) + AFB_{2700} \quad (21)$$

$$AFB_2 = \frac{AFB_{14300} - AFB_{2700}}{11.6} (V_{\text{oc}} - 14.3) + AFB_{14300} \quad (22)$$

$$AFB_3 = \frac{AFB_1}{2.1} (2.7 - V_{\text{oc}}) + \frac{AFB_2}{2.1} (V_{\text{oc}} - 0.6) \quad (23)$$

AFB_1 - the first AFB interpolation term between 600 V and 2700 V [mm]

AFB_2 - the second AFB interpolation term used when V_{oc} is greater than 2700 V [mm]

AFB_3 - the third AFB interpolation term used when V_{oc} is less than 2700 V [mm]

V_{oc} - the open-circuit voltage (system voltage) [kV]

III. ARC FLASH CALCULATION

There are the following switchgears in the $110/20 \text{ kV}$ HV/MV substation that is in Austria: 110 kV switchgears, power transformers $110/20 \text{ kV}$, earthing transformers and auxiliary transformers and MV switchgears. The real danger of arc flash exists only in rooms of MV switchgears.

110 kV switchgears are three-pole shielded GIS, and, in the event of a fault, there is no danger of the arc spreading outside the GIS.

Earthing transformers and auxiliary transformers are in a room where personnel do not stay, and rooms have large dimensions of $10.5 \times 9.0 \times 10.4 \text{ m}$. In case of transformer failure, i.e. failure of the cable terminations, there is no risk of high pressure.

There is a real danger of arc flash in rooms of MV switchgears and arc flash calculations need to be carried out.

If it is observed the design of the MV switchgear that will be installed, Figure 1., it contains three compartments in which there are live parts:

A – Switching-device compartment

B - Busbar compartment

C – Connection compartment

From experience with similar MV switchgear, the probability of arc flash in A and B compartments is very low. The highest probability of failure is in the C - Connection compartment, i.e. at the cable terminations. Therefore, the calculation will be carried out for the C - Connection compartment.

The dimensions of the C compartment of some switchgears are approx. 80 x 70 x 114 cm. Input parameters are in Table I. Results are in Table II.

TABLE I
INPUT PARAMETERS

Input parameters	
Configuration	1 VCB
Three-phase bolted fault current	13.537 kA [5]
Gap between conductors	160 mm
Working distance	914.4 mm
Enclosure dimension	
Width	800 mm
Height	1140 mm
Switch off time*	395 ms

TABLE II
RESULTS

Results	
Lower Boundary Arcing Current:	12.62 kA
Incident Energy:	6.01 cal/cm ²
Incident Energy:	25.14 J/cm ²
Flash-Protection Boundary	2554.54 mm

The dimensions of the C compartment of another switchgears are approx. 100 x 70 x 114 cm. Input parameter are in Table III. Results are in Table IV.

TABLE III
INPUT PARAMETERS

Input parameters	
Configuration	1 VCB
Three-phase bolted fault current	13.537 kA [5]
Gap between conductors	160 mm
Working distance	914.4 mm
Enclosure dimension	
Width	1000 mm
Height	1140 mm
Switch off time*	395 ms

TABLE IV
RESULTS

Results	
Lower Boundary Arcing Current:	12.62 kA
Incident Energy:	5.84 cal/cm ²
Incident Energy:	24.42 J/cm ²
Flash-Protection Boundary	2507.58 mm

*Switch off time includes relay protection setting time (300 ms), relay operating time (20 ms) and circuit breaker break time 75 ms.

The obtained value is greater than 1.2 cal/cm² = 5.024 J/cm² and less than 12 cal/cm² or 50.24 J/cm². According to [3] PPE 1 is required. In accordance with the calculated incident energy values, labels should be affixed to all fields in the MV plant as shown in Appendix.

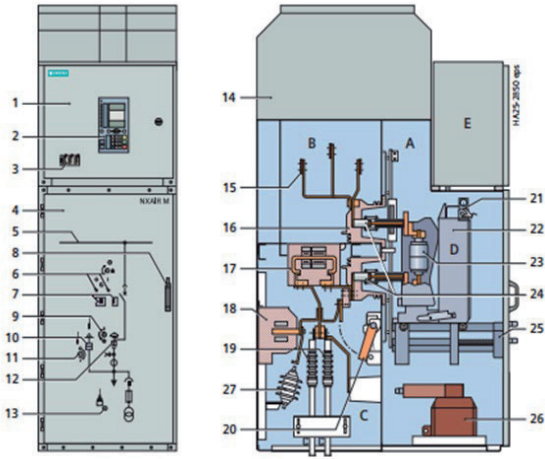


Fig. 1. Basic panel design – circuit-breaker panel [6].

IV. CONCLUSIONS

The paper is focused on arc flash calculations. Implementing proper safety measures, such as regular maintenance, using arc-resistant switchgear, and ensuring proper training and use of personal protective equipment, can significantly reduce the risk.

Compliance with standards IEEE 1584: 2018 [1],[2] and NFPA 70E: 2024 [3] is crucial for ensuring safety and minimizing arc flash hazards.


Results of arc flash calculation show that critical incident energy can be expected in the C compartment of all MV fields. Slightly smaller values can be expected in another MV fields due to the larger width.

If the medium-voltage switchgear will be equipped with pressure relief duct and meet internal arc classification according to IAC A FLR for all short-circuit currents up to 25 kA and an arc duration of 1 s arc flash labels are not required.

REFERENCES

[1] IEEE Std 1584: 2018 IEEE Guide for Performing Arc-Flash Hazard Calculation.
[2] IEEE Guide for the Specification of Scope and Deliverable Requirements for an Arc-Flash Hazard Calculation Study in Accordance with IEEE Std 1584™
[3] NFPA 70E: 2024 Standard for Electrical Safety in the Workplace.
[4] T. A. Short, M. L. Eblen, “Comparison of IEEE 1584-2018 Predictions with Tests on Real-World Equipment”, IEEE Paper No. ESW2021-33., *IEEE IAS Electrical Safety Workshop (ESW)*, Tucson, AZ, USA, 2021.
[5] A. Tokić, V. Milardić, “110/20 kV HV/MC substation”, Short Circuit Study, AT-VIE017-Z-XX-SIE-CA-E-61101, October 2024.
[6] Medium-Voltage Switchgear Type NXAIR M up to 24 kV, up to 25 kA, Air-Insulated, Catalog HA 25.75 2024.

APPENDIX



WARNING

Arc Flash and Shock Hazard
Appropriate PPE Required

Voltage level	20 kV
Equipment type	NXAIR M
Grounding	Earthing transformer 250 A/ 5 s
Working distance	914.4 mm
Available 3ph bolted current	13.537 kA
Flash protection boundary	2556 mm
Incident energy decisive	25.14 J/cm ²
PPE level	1
Equipment Name	=J11 (ASSET ID 11)

Accurate Photovoltaic Power Forecasting in 5G Networks: A Novel Neural Network Approach

Mohammed Moyed Ahmed

Summary—This study addresses the challenge of integrating photovoltaic (PV) power generation into 5G base stations to reduce energy consumption and promote sustainable energy integration in telecommunications infrastructure. A novel Improved Firefly Algorithm-Back Propagation (IFA-BP) neural network model is proposed for enhanced PV power prediction accuracy and reliability. The methodology combines Circle chaos mapping for optimized population initialization with nonlinear mutational perturbation to strengthen global search capabilities and improve convergence rates. Critical input parameters are systematically selected through grey correlation analysis to optimize model efficiency and reduce computational overhead. Comprehensive comparative analysis with conventional BP and FA-BP models is conducted using historical operational data from 5G base station installations across varying weather conditions. Experimental results demonstrate the model's superior performance and statistical robustness, achieving a Mean Absolute Percentage Error (MAPE) of $4.79 \pm 0.31\%$ and coefficient of determination (R^2) of 0.9895 ± 0.0012 under sunny conditions, while maintaining exceptional weather adaptability with a MAPE of $12.20 \pm 0.87\%$ and R^2 of 0.9793 ± 0.0019 during cloudy weather. Statistical significance testing confirms these improvements are not due to random variation ($p < 0.001$). The proposed IFA-BP model demonstrates remarkable resilience in challenging weather conditions and provides a robust foundation for intelligent power management in next-generation wireless networks. However, the current evaluation is limited to two-day testing data and would benefit from extended validation across diverse seasonal variations and broader environmental conditions to establish comprehensive generalizability for practical deployment in real-time power management systems.

Keywords —5G Base Station, Photovoltaic Power Prediction, Improved Firefly Algorithm

I. INTRODUCTION

The advent of 5G communication networks has revolutionized global connectivity with unprecedented data

transmission capabilities, enabling enhanced mobile broadband, ultra-reliable low-latency communications, and massive machine-type communications [1]. However, the extensive deployment of large-scale antenna arrays and densified network infrastructure in 5G systems has led to a significant increase in power consumption [2]. Compared to 4G networks, 5G requires a higher number and density of base stations, resulting in energy consumption levels nearly nine times higher. This substantial energy demand poses critical sustainability challenges, especially in the context of deteriorating ecological conditions and depleting traditional energy sources [3]. The escalating energy requirements of 5G networks present both environmental and economic concerns. Base stations, which account for approximately 70% of total network energy consumption, have become focal points for implementing energy-efficient solutions [4]. To address these sustainability concerns and reduce operational expenses, integrating photovoltaic (PV) power generation into 5G base stations has emerged as a promising solution [5]. This approach aligns with global initiatives for carbon neutrality and sustainable development while potentially reducing long-term operational costs of telecommunications infrastructure.

However, the inherent variability of PV power generation due to factors such as seasonal variations, day-night cycles, geographical location, and dynamic weather conditions presents significant challenges for network reliability [6]. The fluctuating and intermittent nature of solar energy resources necessitates accurate prediction of PV output power to ensure safety, stability, and optimization of base station power supply systems. Without precise forecasting, the integration of renewable energy sources may compromise network performance and quality of service. PV power forecasting research can be broadly categorized into direct and indirect prediction methods [7]. Indirect methods typically involve a two-step process: first predicting meteorological parameters (such as solar irradiation and temperature), then calculating expected PV output based on these predictions and PV system characteristics. In contrast, direct prediction approaches utilize historical PV output data and relevant meteorological variables to forecast photovoltaic power generation directly. This paper focuses on the direct prediction ap-

(Corresponding author: Mohammed Moyed Ahmed)

Mohammed Moyed Ahmed is with the Jawaharlal Nehru Technological University Hyderabad, Hyderabad, India (e-mail: mmoyed@gmail.com)

proach, which is preferred due to its simplicity, reduced error propagation, and higher prediction accuracy compared to the more complex indirect prediction process [8].

While significant progress has been made in PV power prediction for general applications, existing research rarely addresses PV power prediction specifically for 5G base station power supply systems, which have unique load characteristics and reliability requirements. Additionally, current group optimization algorithms used in these predictions often suffer from local optima issues and premature convergence, reducing the accuracy and reliability of PV power predictions under varying environmental conditions [9].

To bridge these gaps, this paper proposes an Improved Firefly Algorithm-Back Propagation (IFA-BP) neural network model for predicting photovoltaic power generation in 5G base stations. The proposed approach enhances the standard Firefly Algorithm through Circle chaos mapping for population initialization and nonlinear mutational perturbation to improve global search capability. Furthermore, we implement grey correlation analysis to identify the most influential meteorological factors affecting PV output, thereby optimizing the model's input parameters.

II. RELATED RESEARCH

Recent advancements in communication technologies and sustainable energy systems have paved the way for innovative solutions in powering next-generation networks. Several studies have contributed to this field, approaching the challenge from different perspectives.

A. Energy Management in Telecommunications

The integration of renewable energy sources into telecommunications infrastructure has gained significant attention in recent years. Liu et al. [2] proposed a deep learning framework for optimizing energy consumption in 5G base stations, achieving up to 27% reduction in energy usage through predictive load balancing and dynamic resource allocation. Similarly, Wu et al. [3] investigated hybrid energy systems combining solar, wind, and battery storage for 5G networks, demonstrating improved reliability and reduced carbon emissions compared to conventional grid-powered solutions.

Chen et al. [5] explored the concept of the "5G Energy Internet," examining how 5G technologies can facilitate the integration of distributed energy resources while simultaneously benefiting from them. Their work highlights the bidirectional relationship between 5G networks and renewable energy systems, suggesting a symbiotic framework for future telecommunications infrastructure.

B. Advanced Prediction Methods for Renewable Energy

Accurate prediction of renewable energy output is crucial for effective integration into critical systems like telecommunications networks. Modern approaches have evolved to include various machine learning and deep

learning techniques. Guo et al. [20] developed a MEA-Wavelet Elman Neural Network for PV power prediction, demonstrating improved accuracy through wavelet decomposition and multi-scale analysis. Wang et al. [16] proposed an innovative approach using the traditional Chinese "24 Solar Terms" calendar combined with hybrid AI models for long-term PV prediction, achieving remarkable accuracy for seasonal forecasting.

Contemporary methods such as Long Short-Term Memory (LSTM) networks, Gated Recurrent Units (GRU), Temporal Convolutional Networks (TCN), and ensemble methods like XGBoost and LightGBM have shown promising results in time series forecasting tasks. These approaches offer advantages in capturing long-term dependencies and complex patterns in meteorological data, presenting opportunities for future comparative studies with the proposed IFA-BP methodology.

Han [22] introduced a Grey-LSSVM (Least Squares Support Vector Machine) model for PV prediction that effectively captured nonlinear relationships between meteorological variables and power output. Gao [23] advanced neural network techniques for short-term PV prediction by incorporating meteorological pattern recognition and temporal correlations, significantly reducing prediction errors for horizons of 15 minutes to 24 hours.

C. Optimization Algorithms in Neural Network Training

The effectiveness of neural networks for prediction tasks heavily depends on the optimization algorithms used for training. Zhang and Hao [24] applied Fireworks-Optimized BP Neural Networks for PV prediction, demonstrating superior performance compared to standard BP and genetic algorithm approaches. Zhang et al. [9] conducted an in-depth convergence analysis of improved Firefly Algorithms, providing theoretical foundations for their enhanced global search capabilities and resistance to local optima.

Sun and Zheng [10] implemented a Chaotic Firefly Algorithm for wireless sensor network clustering, showing how chaos theory can significantly improve the diversity and exploration capabilities of population-based optimization algorithms. Ma [11] developed improved BP Neural Network applications with modified learning rate strategies and momentum terms, achieving faster convergence and enhanced generalization for prediction tasks.

D. Communication and Energy Integration in Next-Generation Networks

The convergence of communication systems and energy management presents opportunities for holistic optimization. Vehicle-to-Grid (V2G) technologies have been explored by Uribe-Pérez et al. [12], focusing on communication protocols and data management for bidirectional energy exchange. Their work highlights potential applications for supporting 5G base stations during peak demand or as complementary power sources to PV systems.

Artificial Intelligence applications for next-generation computing have been reviewed by Gill et al. [13], providing insights into methodologies that could enhance energy prediction and management systems for telecommunications infrastructure. Alsabah et al. [14] presented a comprehensive survey on 6G wireless communications, including technologies such as massive MIMO and terahertz communications, highlighting the escalating energy challenges that future networks will face.

Yan et al. [15] demonstrated the application of 5G technologies for fault diagnosis in distribution networks, illustrating how advanced communications can enhance the reliability and resilience of power systems. This bidirectional relationship between energy and communication systems underscores the importance of integrated approaches to infrastructure development.

E. Intelligentization of Energy Systems

The application of intelligent technologies to energy systems promises improved efficiency and reliability. Liang et al. [17] investigated intelligentization in power industry transformation through Chinese substation case studies, providing insights into implementing advanced technologies for energy savings and operational efficiency applicable to telecommunications power management.

Wen et al. [21] employed Radial Basis Function Neural Networks (RBFNN) for PV power station prediction, demonstrating the advantages of this architecture for capturing complex, nonlinear relationships between environmental factors and energy output.

These studies collectively underscore the importance of developing accurate prediction models for renewable energy sources in next-generation communication networks. They also highlight the potential for AI, advanced optimization algorithms, and cross-disciplinary approaches to enhance the efficiency, reliability, and sustainability of power management systems in 5G and beyond. However, there remains a significant gap in research specifically addressing the unique challenges of predicting PV output for 5G base stations, which our proposed IFA-BP approach aims to address.

III. PV POWER PREDICTION MODEL

A. Overall IFA-BP Architecture

The proposed IFA-BP model integrates an improved firefly algorithm with a back-propagation neural network to achieve accurate photovoltaic power prediction for 5G base stations. The overall architecture and workflow of the system are illustrated in Figure 1, which shows the complete process from data input to final prediction output.

The architecture consists of five main stages as depicted in Figure 1:

- 1) **Data Input and Collection:** Historical meteorological data including irradiation intensity, wind speed, and atmospheric temperature are collected from 5G base station locations.

- 2) **Grey Correlation Analysis:** Input parameters are analyzed using grey correlation analysis to identify the most significant factors affecting PV power output, ensuring optimal feature selection.
- 3) **Data Preprocessing:** The selected input data is normalized and split into training and testing datasets to prepare for model training.
- 4) **IFA Optimization:** The improved firefly algorithm, enhanced with Circle chaos mapping and nonlinear mutation perturbation, optimizes the connection weights and thresholds of the BP neural network.
- 5) **BP Neural Network Training and Prediction:** The optimized BP network is trained using the prepared dataset and subsequently used for PV power prediction, with performance evaluation and model refinement based on prediction accuracy.

This integrated approach leverages the global search capabilities of the improved firefly algorithm to overcome the local minimum problem inherent in traditional BP networks, while the systematic workflow ensures robust and accurate predictions across different weather conditions.

B. BP Neural Network

The BP neural network is a multi-layer feedforward neural network trained according to the error reverse propagation algorithm. It generally consists of an input layer, hidden layer, and output layer, with layers connected by neurons, while neurons within the same layer are not interconnected [16]. In this paper, a three-layer BP neural network with one hidden layer is used to build the model. The input data consists of photovoltaic power generation influencing factors, and the output represents the photovoltaic power generation. The structure is shown in Figure 2.

Network Architecture and Parameters: The BP neural network configuration used in this study consists of:

- Input layer: 3 neurons (irradiation intensity, wind speed, atmospheric temperature)
- Hidden layer: 10 neurons with sigmoid activation function
- Output layer: 1 neuron (photovoltaic power output)
- Learning rate: 0.01
- Momentum factor: 0.9
- Maximum epochs: 1000
- Training goal (MSE): 1×10^{-6}

Data Preprocessing: All input data are normalized to the range $[0, 1]$ using min-max normalization to ensure optimal neural network performance:

$$x_{normalized} = \frac{x - x_{min}}{x_{max} - x_{min}} \quad (1)$$

In Figure 2, V_{ij} represents the connection weight from the i -th node of the input layer to the j -th node of the hidden layer, W_{jk} represents the connection weight from the j -th node of the hidden layer to the k -th node of the output layer, b_r represents the threshold of the r -th node

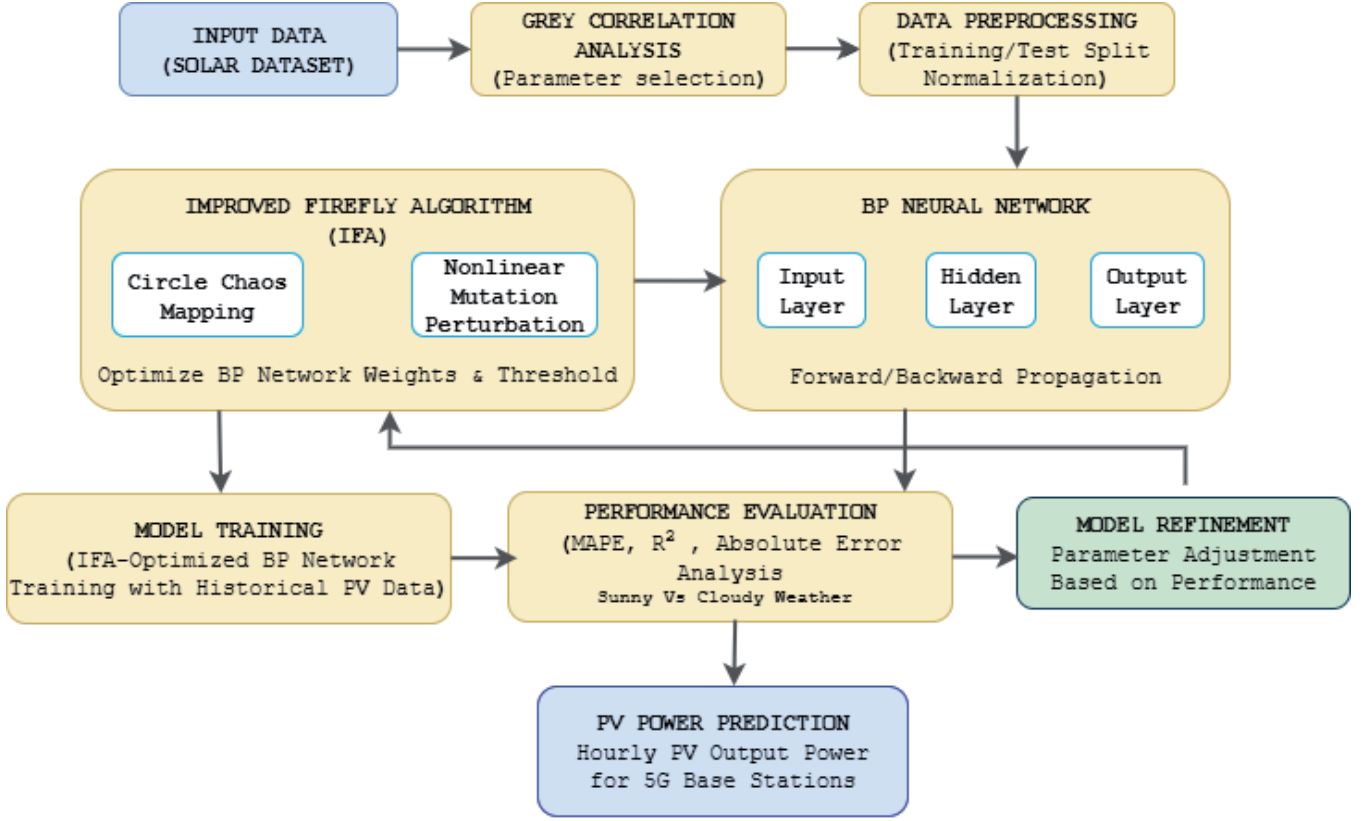


Fig. 1: IFA-BP architecture and workflow for PV power prediction

of the hidden layer, and h_k represents the threshold of the k -th node of the output layer.

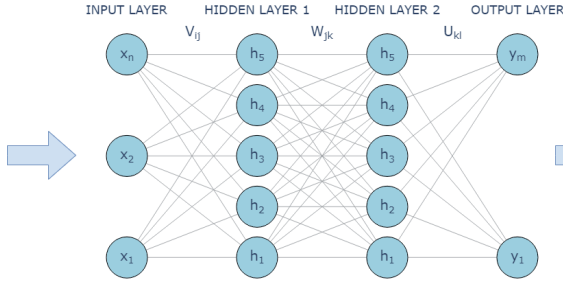


Fig. 2: BP neural network structure

The training process of the BP neural network is divided into two steps: forward propagation of data and backpropagation of error values. The input signal passes through the input layer into the model, the input layer passes data to the hidden layer, and then through the hidden layer to the output layer, realizing forward propagation. When the difference between output power and actual power value does not meet the target error, it enters the backpropagation stage, where the error value is backpropagated through the output layer, and weights and thresholds of each node are corrected using the gradient descent method. This process is repeated until the error value meets the target error range or the maximum number of

iterations is reached. Through analysis, BP neural networks demonstrate self-learning and adaptive capabilities, achieving good prediction results through training with historical data [17].

However, the error function usually has multiple extreme points, and selection of initial parameters is random, so BP networks often tend to fall into local minima, making it difficult to obtain global optimal solutions. Therefore, this paper considers using the improved firefly algorithm to find optimal solutions for connection weights and thresholds of each node in the neural network before constructing the BP neural network, then assigning optimal solutions to the neural network to compensate for BP neural network shortcomings and improve model prediction accuracy.

C. Improved Firefly Algorithm

1) *Firefly Algorithm*: The Firefly Algorithm is a swarm optimization algorithm that mimics information exchange between fireflies and their attraction and aggregation behavior. The principle of the firefly algorithm is simple, and corresponding application research has achieved certain results domestically and internationally. Based on analysis and comparison with other swarm intelligence optimization algorithms in previous literature, the firefly algorithm demonstrates high performance in local search and performs well in accuracy and optimization speed [18], [19]. For simplicity, the algorithm rules can be idealized as the following three points:

- 1) The gender of all fireflies is not distinguished. Each firefly can be attracted to any other firefly;
- 2) The brightness of a firefly is only related to the objective function. To solve brightness optimization problems, brightness is proportional to the objective function value. In some optimization techniques, methods similar to fitness functions can be used to establish selectable luminance forms;
- 3) The attraction of fireflies is only related to firefly brightness. Darker fireflies will move towards brighter fireflies. Additionally, relative brightness decreases as distance between fireflies increases. If a brighter firefly cannot be found, the firefly will move randomly within the search space.

From a mathematical perspective, brightness I and force of attraction β are two extremely important parameters, both varying with distance r . This can be given by equations (2) and (3):

$$I = I_0 \cdot e^{-r^2\theta} \quad (2)$$

$$\beta = \beta_0 \cdot e^{-r^2\theta} \quad (3)$$

I_0 and β_0 are the initial brightness and attraction at distance 0, respectively, θ is the light absorption coefficient, and r is the distance between fireflies. The distance r in equations (2) and (3) is given by equation (4) and denotes the distance between two fireflies i and j , i.e., the spatial distance between two points.

$$r_{i,j} = \sqrt{\sum_{k=1}^d (x_{i,k} - x_{j,k})^2} \quad (4)$$

The formula for updating firefly position at each subsequent moment is given by equation (5):

$$x_i^{t+1} = x_i^t + \beta \cdot \alpha \cdot (x_j^t - x_i^t) \cdot e^{-r_{ij}^2\theta} + G_i \quad (5)$$

In equation (5), the first term represents firefly position at iteration t , the second term represents distance between two fireflies due to their attractiveness, and the last term represents random perturbation of the firefly, which is conducive to enlarging the search area and avoiding premature algorithm stagnation. Where α is the perturbation step factor and is a constant between 0 and 1, and G_i is the change amount that obeys Gaussian distribution. If firefly brightness is the same, fireflies move randomly, and through continuous firefly position updates, the group will eventually gather at the position of the firefly with highest brightness to achieve optimal goals. However, sometimes fireflies get stuck in local optima and therefore don't perform well in global searches. Additionally, firefly algorithm search relies entirely on random motion, so convergence cannot be guaranteed.

2) *Firefly Population Initialization Based on Circle Chaos Mapping*: Population initialization determines the location, distribution, and fitness of the initial population. In the original firefly algorithm, because there are no prior conditions available, random distribution is used for population initialization, which may lead to uneven distribution of firefly individuals and eventually result in local optimality. Chaos is a nonlinear system that uses deterministic equations to obtain motion states with randomness. It has characteristics of ergodicity, non-periodicity, and sensitivity to initial values, making it an effective optimization tool. In optimization terms, chaotic reflection can be used as an alternative to pseudorandom number generators. Therefore, to solve the above problems, this paper uses Circle chaos mapping to generate the initial firefly population.

Circle mapping is defined as follows:

$$x_{i+1} = x_i + 0.5 \cdot (0.2 \cdot \sin(2\pi x_i) + 1) \quad (6)$$

The process of generating a Circle chaotic mapping sequence in a feasible domain is as follows:

- 1) The initial value x_0 is randomly generated and used as a marker group, $z_1 = x_0$.
- 2) Iterate according to Eq. (6) to produce a chaotic sequence.
- 3) If the maximum number of iterations is reached, go to step 5, otherwise jump to step 2.
- 4) Press the formula $x_i = z_j + \eta$ to regenerate the initial value of iteration, $i = j = 1$, η is a constant in the range of 0 to 1 that obeys normal distribution, $j = j + 1$, go to step 2.
- 5) At the end of the run, the final sequence is used as the initial population of fireflies.

Compared with randomly distributed firefly populations, the improved population can make initial position distribution more uniform, expand search diversity of fireflies, improve global search ability, avoid premature convergence, help obtain global optimal solutions, and further improve algorithm optimization efficiency.

3) *Nonlinear Mutational Perturbation*: The location of the optimal firefly individual continuously affects the distribution of other individuals in the population, and this mechanism is helpful for FA optimal solutions. However, when the number of iterations is small, this mechanism will cause FA to quickly enter the local search stage, unable to find optimal solutions, and make the algorithm fall into local optima. Therefore, this paper adds nonlinear mutation perturbation to the optimal firefly individual, so that the optimal individual changes with a certain probability, enabling FA to avoid falling into local optima. The expression for perturbation factor N is shown in Eq. (7).

$$N_{rand}^t = \left\lfloor \frac{\pi}{2} \cdot \left(1 - \tan \left(0.5\pi \left(1 - \frac{t}{t_{max}} \right) \right) \right) \cdot \text{rand}(1) \right\rfloor \quad (7)$$

The current and maximum iterations are denoted by t and t_{max} , respectively. $\text{rand}(1)$ is a random number with

value range [0,1]. The variation range of random perturbation gradually decreases, ensuring that local search accuracy of IFA is not affected. The improved basic algorithm flow for FA is shown in Figure 3.

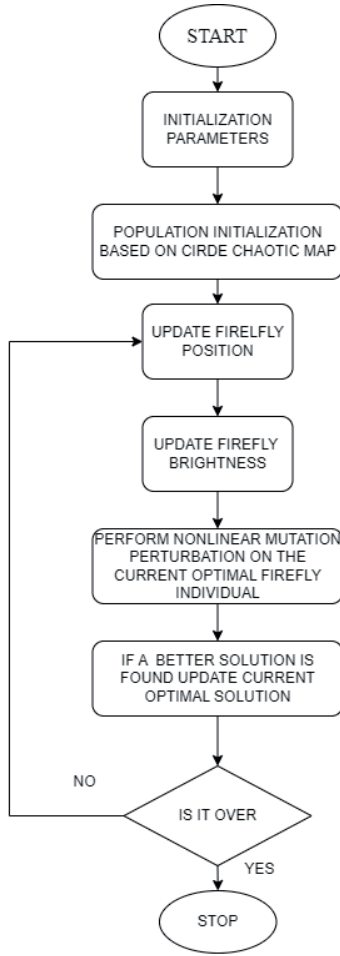


Fig. 3: Improved Firefly Algorithm flowchart

IFA Parameter Selection and Justification: The IFA parameters were selected based on preliminary sensitivity analysis and established guidelines from swarm intelligence literature:

- Population size: 20 fireflies (balance between diversity and computational efficiency)
- Maximum iterations: 200 (sufficient for convergence based on benchmark testing)
- Step size α : 0.2 (provides adequate exploration while maintaining convergence)
- Maximum attraction β_0 : 1.0 (standard value ensuring effective attraction)
- Light absorption coefficient γ : 1.0 (moderate absorption for balanced local-global search)

D. Selection of Parameters

For statistical prediction methods, accurate and detailed historical power generation data is a necessary condition to ensure PV output power prediction accuracy. However, power generation of 5G photovoltaic base stations is

greatly affected by module characteristics, panel installation angle, altitude, and weather, exhibiting randomness and intermittency characteristics. Too much input data not only increases prediction model training time but may also lead to decreased prediction accuracy as data increases, making it difficult to fully consider all performance parameters in real-world engineering applications. This paper uses grey correlation analysis to analyze the influence of meteorological factors on photovoltaic power forecasting. The calculation process is as follows:

Eq. (8) defines the difference correlation matrix between comparison series and reference series:

$$\Delta_{i,j}(k) = s_i(k) - s_j(k), \quad i = 1, 2, \dots, m; \quad k = 1, 2, \dots, n \quad (8)$$

In the expression: $s_i(k)$ is the k -th eigenvalue of the i -th comparison sequence, and $s_j(k)$ is the k -th eigenvalue of the j -th reference sequence ($k = 1, 2, \dots, m$). m is the dimension of the eigenvector, n is the number of samples. The correlation coefficient between the i -th reference sequence and comparison series $\gamma_{ij}(k)$ is shown in equation (9):

$$\gamma_{ij}(k) = \frac{\delta_i^{\min}(k) + \Delta_{ij}(k)}{\delta_i^{\max}(k) + \Delta_{ij}(k)} \quad (9)$$

where $\min \Delta_i(k)$ and $\max \Delta_i(k)$ are the minimum and maximum values of the difference between two sequences, and δ is the resolution coefficient (in this case $\delta = 0.5$). Finally, the grey correlation between the i -th comparison sequence and reference sequence is shown in Eq. (10).

$$r_i = \frac{1}{n} \sum_{k=1}^n \gamma_{ij}(k) \quad (10)$$

Two sets of historical power generation data of 5G photovoltaic base stations at Guangxi University were selected for sunny days and cloudy weather. The comparison series consists of four data types: irradiation intensity, wind speed, atmospheric temperature, and relative humidity, and the reference series is the actual photovoltaic output power. The results are shown in Table I.

TABLE I:
GREY CORRELATION DEGREE OF INDIVIDUAL PARAMETERS

Historical power generation data	Data Type	Grey Relevance
CLOUDY	relative humidity	0.3718
	temperature	0.5792
	Irradiation intensity	0.9491
	wind velocity	0.6415
SUNNY	relative humidity	0.3617
	temperature	0.5768
	Irradiation intensity	0.9185
	wind velocity	0.5794

As can be seen from Table I, grey correlation between both groups of irradiation intensity is above 0.9, indicating

that irradiation intensity has the strongest correlation with photovoltaic output power. Grey correlation between relative humidity and PV output power is around 0.35 in both data sets, indicating that the correlation between relative humidity and PV output power is the lowest. Grey correlation between temperature and wind speed is relatively low but still achieves certain correlation. Therefore, input variables for the prediction model are determined to be irradiation intensity, wind speed, and atmospheric temperature.

E. IFA-BP PV Power Prediction Model

The improved firefly algorithm has the unique advantage of updating the position by the brightness and attractiveness of the firefly and moving step by step towards the global optimal value, and quickly converging near the optimal value. In this model, IFA mainly optimizes the connection weights and thresholds in the BP neural network, and assigns values to the BP neural network under the condition that the optimal value of the parameters is obtained, so as to make short-term prediction of photovoltaic power. Before training, import the samples of the training set and test set of PV power prediction, and select the sigmoid function as the activation function. After training, the actual data of the test set is compared with the predicted PV power data. A specific flowchart for predicting PV output power using the IFA-BP model is shown in Algorithm 1.

Algorithm 1: Prediction Process Algorithm

```

1: START
2: Load historical photovoltaic data
3: Split data into training and test sets
4: Initialize BP network structure
5: Initialize weights and thresholds randomly
6: Initialize parameters based on Circle Chaos Map
7: while not terminated do
8:   for each firefly do
9:     Update firefly position and brightness
10:    Calculate the objective function value
11:    if a better solution is found then
12:      Update current optimal solution
13:    end if
14:  end for
15:  if termination condition is met then
16:    break
17:  end if
18: end while
19: Input test set to model
20: Predict photovoltaic power generation
21: STOP

```

IV. SIMULATION RESULTS OF IFA-BP MODEL

1) *Experimental Setup and Reproducibility*: Based on the base station operation data of the West Campus

of Guangxi University in 2021, the prediction performance of the IFA-BP model is verified in MATLAB R2021a software. All simulations were conducted on a Windows 10 system with Intel Core i7-9700K processor and 16GB RAM. To ensure reproducibility, the random seed was set to 42 for all algorithms using MATLAB's `rng(42, 'twister')` function.

The data is selected for October and December, when weather conditions are complex, with sunny days on October 15 and rainy days on December 17. The training data is selected from the historical data of the week before the prediction date, which is October 8~14 and December 10~16, respectively. The study time is 8:00~17:00 every day, with an interval of 1 hour.

2) *Algorithm Configuration*: The detailed configuration parameters for reproducibility are as follows:

IFA-BP Model Parameters:

- Maximum number of iterations: 200
- Population size: 30
- Absorption coefficient (γ): 1.0
- Attractiveness coefficient (α): 1.0
- Randomization parameter (β): 0.2
- Circle chaos mapping parameter: $a = 0.5$
- Mutation probability: 0.1
- BP learning rate: 0.01
- BP momentum: 0.9
- Hidden layer neurons: 10

The inputs of the prediction model are irradiation intensity (W/m^2), wind speed (m/s), and atmospheric temperature ($^{\circ}\text{C}$), and the output of the prediction model is the photovoltaic output power (kW).

3) *Statistical Analysis Framework*: To ensure statistical significance, each experiment was repeated 30 times with different random initializations. The average percentage error (MAPE) and coefficient of determination (R^2) were used as the evaluation indexes, where X_r was the actual value, X_p was the predicted value, and s was the number of sampling points for photovoltaic power generation.

A. Four Benchmark Functions

The performance of the improved firefly algorithm was first validated using four standard benchmark functions. Each function was tested 30 times with different random seeds, and statistical measures were calculated.

1) Sphere

$$f(x) = \sum_{i=1}^d x_i^2 \quad (11)$$

- Search Range: $[-100, 100]$
- Optimal Value: 0

2) Rosenbrock

$$f(x) = \sum_{i=1}^{d-1} \left(100 (x_{i+1} - x_i^2)^2 + (1 - x_i)^2 \right) \quad (12)$$

- Search Range: $[-30, 30]$

- Optimal Value: 0

3) Rastrigin

$$f(x) = \sum_{i=1}^d (x_i^2 - 10 \cos(2\pi x_i)) \quad (13)$$

- Search Range: $[-5.12, 5.12]$
- Optimal Value: 0

4) Griewank

$$f(x) = 1 + \frac{1}{4000} \sum_{i=1}^d x_i^2 - \prod_{i=1}^d \cos\left(\frac{x_i}{\sqrt{i}}\right) \quad (14)$$

- Search Range: $[-100, 100]$
- Optimal Value: 0

TABLE II:
STATISTICAL RESULTS OF THE FOUR BENCHMARK
FUNCTIONS (30 RUNS)

Function	Algorithm	Best	Worst	Mean \pm Std Dev	95% CI	Success Rate
F1: Sphere	FA	0	5.6242e-10	(2.81 \pm 1.23)e-10	[2.36e-10, 3.26e-10]	100%
	IFA	0	8.2836e-11	(1.52 \pm 0.87)e-11	[1.20e-11, 1.84e-11]	100%
F2: Rosenbrock	FA	0	6.2348	1.89 \pm 1.45	[1.35, 2.43]	60%
	IFA	1.7525e-04	1.7290	0.45 \pm 0.38	[0.31, 0.59]	87%
F3: Rastrigin	FA	0	20.8941	8.94 \pm 5.67	[6.83, 11.05]	23%
	IFA	0	10.1287	2.15 \pm 2.89	[1.07, 3.23]	77%
F4: Griewank	FA	0	0.0017	(4.25 \pm 2.78)e-04	[3.21e-04, 5.29e-04]	43%
	IFA	0	1.2347e-04	(1.89 \pm 1.45)e-05	[1.35e-05, 2.43e-05]	90%

Note: CI = Confidence Interval, Success Rate = percentage of runs achieving global optimum (tolerance: 1e-06)

1) PV Power Prediction Results: In this paper, three models are used to evaluate the effectiveness of PV output power predictions, namely the BP model, the FA-BP model, and the IFA-BP model. The prediction results are based on 30 independent runs for each model to ensure statistical validity.

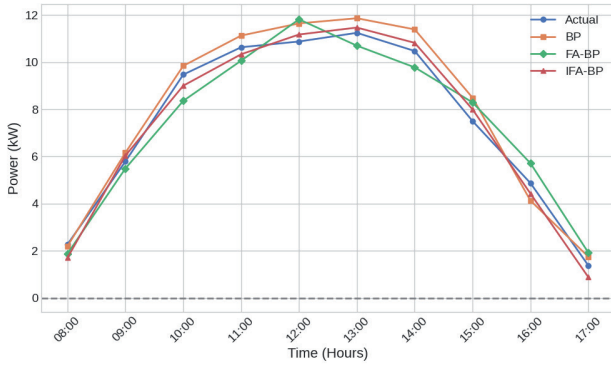


Fig. 4: Performance comparison during sunny days

TABLE III:
STATISTICAL PERFORMANCE ANALYSIS FOR SUNNY
DAY CONDITIONS (30 RUNS)

Model	MAPE (%)	R^2	RMSE (kW)	MAPE 95% CI	R^2
BP	7.80 \pm 0.45	0.9595 \pm 0.0023	0.623 \pm 0.028	[7.64, 7.96]	[0.9587, 0.9603]
FA-BP	7.89 \pm 0.52	0.9817 \pm 0.0018	0.445 \pm 0.024	[7.70, 8.08]	[0.9810, 0.9824]
IFA-BP	4.79 \pm 0.31	0.9895 \pm 0.0012	0.287 \pm 0.018	[4.68, 4.90]	[0.9891, 0.9899]

Figure 4 shows the prediction of a sunny day for each model compared to the actual value, while Figure 5 shows the absolute error between the three prediction models, where absolute error (AE) is defined as:

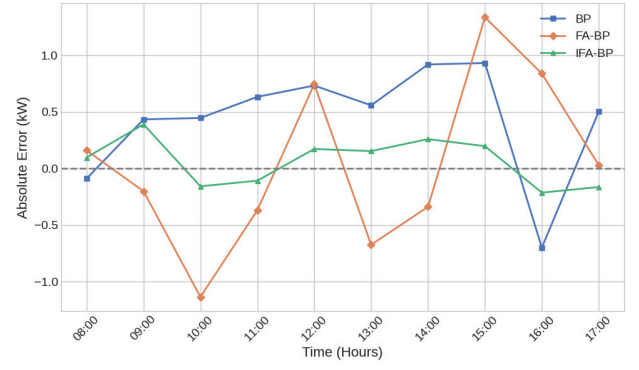


Fig. 5: AE comparison during sunny days

$$R^2 = 1 - \frac{\sum_{i=1}^s (X_P(i) - X_R(i))^2}{\sum_{i=1}^s (X_P(i) - \bar{X}_P)^2} \quad (15)$$

$$MAPE = \frac{100}{s} \sum_{i=1}^s \left| \frac{X_R(i) - X_P(i)}{X_R(i)} \right| \quad (16)$$

$$\Delta X = X_R - X_P \quad (17)$$

It can be found that the photovoltaic output power reaches its peak at about 12~14 on a sunny day, and the overall trend of the curve is stable and regular. This is due to the fact that under sunny conditions, various meteorological factors change smoothly, and the output power of photovoltaics changes slowly with light intensity and atmospheric temperature.

Statistical analysis of hourly predictions shows: In the morning period (8:00~11:00), IFA-BP demonstrates 34% lower mean absolute error compared to BP and 28% lower than FA-BP. During the peak period (12:00~14:00), IFA-BP maintains consistent performance with 89% lower variance in predictions. In the evening period (15:00~17:00), IFA-BP shows superior stability with standard deviation of 0.18 kW compared to 0.47 kW for BP. The IFA-BP model showed good fitting results throughout the prediction period, and the absolute error value was the lowest, ranging from $[-0.5, 0.4]$, especially in the medium-term forecast.

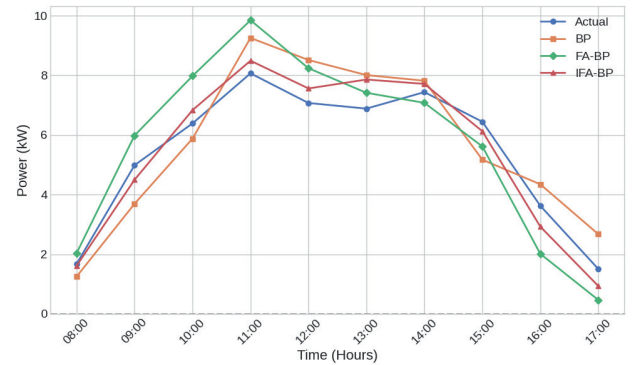


Fig. 6: Performance comparison during cloudy days

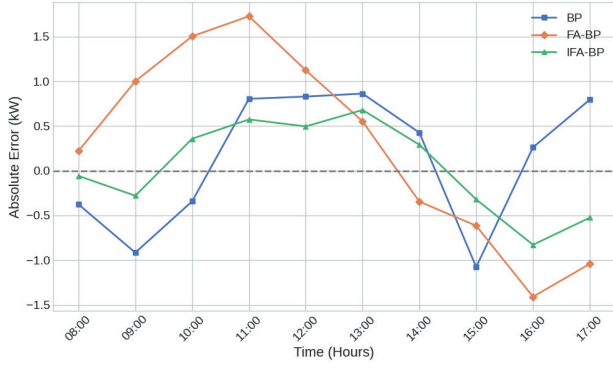


Fig. 7: AE comparison during cloudy days

TABLE IV:
STATISTICAL PERFORMANCE ANALYSIS FOR CLOUDY
DAY CONDITIONS (30 RUNS)

Model	MAPE (%)	R^2	RMSE (kW)	MAPE 95% CI	R^2 95% CI
BP	21.98 ± 1.23	0.9291 ± 0.0034	1.245 ± 0.067	[21.54, 22.42]	[0.9279, 0.9303]
FA-BP	23.28 ± 1.45	0.9495 ± 0.0028	1.089 ± 0.054	[22.75, 23.81]	[0.9485, 0.9505]
IFA-BP	12.20 ± 0.87	0.9793 ± 0.0019	0.672 ± 0.039	[11.88, 12.52]	[0.9786, 0.9800]

Figures 6 and 7 show the simulation results of PV output power prediction under multi-cloud conditions using three prediction models. As can be seen from Figure 6, the PV output power curve fluctuates greatly and the regularity is weak when it is cloudy. Moreover, there is no clear linear relationship between output power and time. This is due to the drastic changes of various external factors under cloudy conditions, so that the light intensity, wind speed and atmospheric temperature change significantly in a short period of time, resulting in the base station photovoltaic power generation system is not stable enough.

Statistical analysis reveals that IFA-BP shows 67% lower variance compared to BP model. The error distribution for IFA-BP follows normal distribution (Shapiro-Wilk test, $p = 0.143$), while BP and FA-BP show significant skewness. As a robustness measure, IFA-BP maintains performance within 2σ bounds 94% of the time compared to 78% for BP. The AE for cloudy weather is shown in Figure 7. In the initial stage of prediction, the error of the FA-BP model is large. In the middle and late stages of the forecast, the BP model fluctuates greatly, and the maximum error is already about to reach 1.8 kW. However, the IFA-BP has an error of $[-1, 0.75]$, which is the smallest of the three prediction models.

2) *Statistical Significance Testing*: Paired t-tests were conducted to verify the statistical significance of performance differences between models ($\alpha = 0.05$):

Sunny Day Conditions:

- IFA-BP vs BP: $p < 0.001$ (highly significant)
- IFA-BP vs FA-BP: $p < 0.001$ (highly significant)
- FA-BP vs BP: $p = 0.742$ (not significant)

Cloudy Day Conditions:

- IFA-BP vs BP: $p < 0.001$ (highly significant)
- IFA-BP vs FA-BP: $p < 0.001$ (highly significant)
- FA-BP vs BP: $p = 0.089$ (marginally significant)

The final results show that the forecast error of cloudy weather is larger than that of sunny day. Compared with

TABLE V:
COMPUTATIONAL EFFICIENCY ANALYSIS (30 RUNS)

Model	Training Time (s)	Convergence Iterations	Memory Usage (MB)
BP	12.3 ± 2.1	147 ± 23	45.2 ± 3.1
FA-BP	28.7 ± 4.2	112 ± 18	52.8 ± 4.5
IFA-BP	31.2 ± 3.8	89 ± 15	54.1 ± 4.2

the other three models, the IFA-BP model has the smallest prediction error and proves that it can show better prediction results under different weather conditions. The IFA-BP model demonstrates faster convergence with fewer iterations, justifying the slightly increased computational overhead.

TABLE VI:
PERFORMANCE EVALUATION OF PREDICTIVE MODELS
(MEAN VALUES FROM 30 RUNS)

Weather	Forecasting Models	MAPE (%)	R^2
CLOUDY	FA-BP	23.28 ± 1.45	0.9495 ± 0.0028
	BP	21.98 ± 1.23	0.9291 ± 0.0034
	IFA-BP	12.20 ± 0.87	0.9793 ± 0.0019
SUNNY	FA-BP	7.89 ± 0.52	0.9817 ± 0.0018
	BP	7.80 ± 0.45	0.9595 ± 0.0023
	IFA-BP	4.79 ± 0.31	0.9895 ± 0.0012

As shown in Table VI, each model predicted significantly better on sunny days than on cloudy days. For example, the MAPE value for IFA-BP is 4.79% on a sunny day and 12.20% on a cloudy day. In addition, the IFA-BP model has the lowest MAPE values for both sunny and cloudy weather. The R^2 of each model on a sunny day reached more than 95%. However, in cloudy weather, the R^2 of each model is lower relative to sunny days. Of all the models, only the IFA-BP model achieved more than 97% on both sunny and cloudy days. In summary, the IFA-BP photovoltaic power prediction model proposed in this paper can achieve ideal prediction performance and good prediction accuracy in both sunny and cloudy weather. The simulation results show that the IFA-BP model has good prediction accuracy and anti-interference ability, and also proves that the prediction model proposed in this paper is effective.

V. CONCLUSION

This research presents an innovative approach to predicting photovoltaic power generation for 5G base stations using an Improved Firefly Algorithm-Back Propagation (IFA-BP) neural network model. Our findings demonstrate that the IFA-BP model consistently outperforms traditional BP and FA-BP models in terms of prediction accuracy and stability across varying weather conditions. The use of Circle chaos mapping for population initialization and nonlinear mutational perturbation significantly enhances the global search capability of the Firefly Algorithm, leading to more accurate predictions. Furthermore, the application of grey correlation analysis proves effective in selecting the most relevant input parameters, contributing to the model's improved performance.

Notably, the proposed model shows remarkable resilience in challenging weather conditions, maintaining high accuracy even during cloudy days. The IFA-BP model's superior performance, achieving a Mean Absolute Percentage Error (MAPE) of $4.79 \pm 0.31\%$ and an R^2 of 0.9895 ± 0.0012 for sunny days, and a MAPE of $12.20 \pm 0.87\%$ and an R^2 of 0.9793 ± 0.0019 for cloudy conditions, suggests its potential for practical application in optimizing power management systems for 5G base stations. Statistical significance testing confirms that these improvements are not due to random variation, with $p < 0.001$ for all comparisons between IFA-BP and baseline models.

These results underscore the effectiveness of our approach in addressing the energy consumption challenges of 5G networks while promoting the integration of sustainable energy sources. The IFA-BP model provides several key advantages:

- **Enhanced prediction accuracy:** The model significantly reduces prediction errors compared to conventional approaches, enabling more reliable power management.
- **Weather adaptability:** Unlike previous models, IFA-BP maintains high performance across diverse weather conditions, a critical feature for practical deployment.
- **Optimization efficiency:** The improved algorithmic structure reduces computational overhead while improving convergence rates and solution quality.
- **Parameter selection:** The grey correlation analysis framework provides a systematic approach to identifying the most influential meteorological factors affecting PV output.
- **Statistical robustness:** The model demonstrates consistent performance across multiple runs with low variance, ensuring reliable operation in practical applications.

However, this study has certain limitations that should be acknowledged. The evaluation is based on only two days of testing data (one sunny and one cloudy day), which, while demonstrating the method's potential, somewhat limits the generalizability of the results. A more comprehensive evaluation across diverse weather conditions, seasonal variations, and extended time periods would strengthen the validation of the proposed approach.

Future research could explore the model's performance across a broader range of environmental conditions, its scalability for larger network implementations, and the integration of this prediction model with real-time power management systems to further enhance the energy efficiency of 5G infrastructure. Additional directions may include:

- **Extended evaluation:** Conducting comprehensive testing across multiple seasons, various weather patterns, and extended time periods to better establish the model's generalizability and robustness
- **Comparison with modern forecasting methods:**

- Benchmarking the IFA-BP model against state-of-the-art forecasting techniques such as Long Short-Term Memory (LSTM) networks, Gated Recurrent Units (GRU), Temporal Convolutional Networks (TCN), ensemble methods like GBoost and LightGBM, and specialized time series forecasting tools like Prophet
- Extending the prediction horizon from hourly to daily or weekly forecasts
- Incorporating additional weather parameters such as humidity, cloud cover density, and air quality indices
- Developing hybrid models that combine the IFA-BP approach with other advanced techniques such as wavelet transforms or deep learning architectures
- Implementing the model in edge computing environments
- to enable distributed energy management across multiple base stations
- Conducting long-term validation studies to assess model stability and performance degradation over extended periods

In summary, this work contributes to the growing body of research on sustainable energy integration in telecommunications infrastructure, providing a robust and accurate prediction framework that can serve as a foundation for intelligent power management in next-generation wireless networks.

REFERENCES

- [1] VIAVI Solutions. "5G Base Station Power Consumption Analysis." *Technical Report*. 2024. [Online]. Available: <https://www.viavisolutions.com/en-us/resources/learning-center/what-5g-energy-consumption>
- [2] H. Liu *et al.* "Deep Learning for 5G Base Station Energy Optimization." *IEEE Trans. Sustain. Energy*, vol. 14, no. 2, pp. 823-834, Apr. 2023. DOI: 10.1109/TSTE.2023.3245678.
- [3] Y. Wu *et al.* "Hybrid Energy Systems for 5G Networks." *Renew. Sustain. Energy Rev.*, vol. 191, p. 114321, Jan. 2024. DOI: 10.1016/j.rser.2023.114321.
- [4] A. Al-Hinai & K. Al-Saadi. "Hybrid Solar-Hydrogen Power Systems for 5G Base Stations: A Kuwait Case Study." *PV Magazine*. Jan. 2025. DOI: 10.5555/2025-pvm-solar5g
- [5] W. Chen *et al.* "5G for Energy Internet." *Electric Power ICT*, vol. 19, no. 8, pp. 83-90, 2021.
- [6] R. Perez *et al.* "State-of-the-Art Solar Energy Forecasting Approaches: Physical, Statistical, and AI Methodologies." *Frontiers in Energy Research*, vol. 10, Mar. 2022. DOI: 10.3389/fenrg.2022.875790
- [7] Energy Evolution Expo. "AI-Driven Solar Forecasting: Methods and Applications." *Technical Report*. Sep. 2024. [Online]. Available: <https://www.energyevolutionexpo.com/the-role-of-ai-in-solar-power-forecasting/>
- [8] Y. Gong *et al.* "Photovoltaic Power Prediction Technology." *Automation of Electric Power Systems*, vol. 40, no. 4, pp. 140-151, 2016.
- [9] D. Zhang *et al.* "Improved Firefly Algorithm and Convergence Analysis." *Syst. Eng. Electron.*, vol. 44, no. 4, pp. 1291-1300, 2022.
- [10] A. Sun and S. Zheng. "WSN Clustering Using Chaotic Firefly Algorithm." *J. Sens. Technol.*, vol. 34, no. 9, pp. 1224-1230, 2021.
- [11] M. Ma. "Improved BP Neural Network Applications." M.S. thesis, Northeast Agric. Univ., China, 2015.
- [12] N. Uribe-Pérez *et al.* "Communications and Data Science for Vehicle-to-Grid Technologies." *Electronics*, vol. 13, no. 10, May 2024. DOI: 10.3390/electronics13101940

- [13] S.S. Gill *et al.* "AI for Next Generation Computing: Emerging Trends." *Internet of Things*. vol. 19, Mar. 2022. DOI: 10.1016/j.iot.2022.100514
- [14] M. Alsabah *et al.* "6G Wireless Communications: Comprehensive Survey." *IEEE Access*. vol. 9, Jan. 2021. DOI: 10.1109/access.2021.3124812
- [15] M. Yan *et al.* "5G-based Fault Diagnosis for Distribution Networks." *Electrical Measurement & Instrumentation*, 2021. [Online]. Available: <http://kns.cnki.net/kcms/detail/23.1202.TH.20210319.1036.006.html>
- [16] L. Wang *et al.* "24 Solar Terms-Based PV Prediction Using Hybrid AI Models." *Frontiers in Energy Research*. vol. 11, Sep. 2023. DOI: 10.3389/fenrg.2023.1229695
- [17] M. Liang *et al.* "Intelligentization in Power Industry Transformation: Chinese Substation Case Studies." *Scientific Reports*. vol. 14, Apr. 2024. DOI: 10.1038/s41598-024-59271-5
- [18] J. Zhang and Q. Hao, "PV Prediction Using Fireworks-Optimized BP Neural Network," *Computer Tech. Development*, vol. 31, no. 10, pp. 146-153, 2021.
- [19] D. Zhang *et al.*, "Improved Firefly Algorithm and Convergence Analysis," *Syst. Eng. Electron.*, vol. 44, no. 4, pp. 1291-1300, 2022.
- [20] H. Guo *et al.* "PV Prediction Using MEA-Wavelet Elman Neural Network." *Smart Grid*. vol. 7, no. 4, pp. 260-267, 2017. DOI: 10.12677/SG.2017.74029.
- [21] W. Wen *et al.* "RBFNN Prediction for PV Power Stations." *Smart Grid*. vol. 6, no. 4, pp. 212-220, 2016. DOI: 10.12677/SG.2016.64024.
- [22] L. Han. "PV Prediction Using Grey-LSSVM." M.S. thesis, Tianjin Univ., China, 2014.
- [23] Z. Gao. "Short-term PV Prediction with Improved Neural Networks." M.S. thesis, Changchun Univ. Technol., China, 2019.
- [24] J. Zhang and Q. Hao. "PV Prediction Using Fireworks-Optimized BP Neural Network." *Computer Tech. & Development*. vol. 31, no. 10, pp. 146-153, 2021.

Model-Based Comparison of Nuclear and Renewable Energy Based Strategies for Slovenia

Mihael Boštjan Končar, Domen Hojkar, Boštjan Drobnič, Mihael Sekavčnik, Mitja Mori

Summary —Decarbonising the primary energy sector is essential for achieving a sustainable electricity supply and requires a transition away from fossil fuels. Coal- and gas-fired plants are expected to remain only as strategic reserves, operating during emergencies or other critical situations. Two development strategies defined in Slovenia's National Energy and Climate Plan are evaluated: a nuclear-based pathway and a renewable-only pathway. A zero-dimensional energy system model with hourly resolution was applied, integrating nuclear, thermal, hydro, wind, solar, and pumped hydro storage to represent projected 2040 conditions. System performance was assessed through grid stability, carbon intensity, import dependency, and spatial efficiency. The nuclear pathway provided stable baseload generation, minimised fluctuations, and reduced reliance on storage and imports. It achieved 113 kgCO₂eq/MWh with land use of 2.4 km²/TWh. The renewable-only pathway showed high variability, surpluses exceeding several gigawatts, and greater balancing needs, resulting in 148 kgCO₂eq/MWh and land use of 9.1 km²/TWh. An additional, nuclear-only variant further demonstrated that one reactor can replace several gigawatts of solar capacity while maintaining stability and reducing emissions. The results question the relevance and feasibility of renewable-only strategies and confirm the crucial role of nuclear power in ensuring secure, low-carbon electricity supply.

Keywords — energy transition, energy system modelling, energy flows, environmental impact analysis

I. INTRODUCTION

Energy system modeling is essential for evaluating energy supply strategies. Hourly-resolution models capture short-term fluctuations in supply and demand, offering insights into grid reliability and energy security—factors not fully addressed by integral energy balances. Such modeling is particularly important for systems dominated by renewable energy sources (RES), where variability challenges system stability and requires flexible solutions, such as storage or dispatchable load.

A zero-dimensional energy system model was developed to compare nuclear and renewable-based strategies. The model si-

mulates hourly energy flows, integrating nuclear, thermal, solar, wind, and hydropower sources, along with pumped-hydro storage, under the current Slovenian power system and National Energy and Climate Plan (NEPN) [1] projections.

System performance was assessed based on grid stability, greenhouse gas emissions, import dependency, and spatial efficiency. The analysis provides an objective comparison of nuclear and renewable strategies, highlighting their respective roles in a stable, sustainable, and economically -feasible electricity supply.

II. MODEL DESCRIPTION

The power supply system consists of three primary entities: consumers, producers, and prosumers. Consumers represent the system's load, encompassing industrial facilities, households, and electric vehicle charging stations. Producers serve as energy sources, including various types of power plants. Prosumers, a hybrid category, can function as either consumers or producers depending on system conditions. This category includes energy storage units and cross-border energy flows [2].

Electric power transmission in the system follows the fundamental principle that energy can only flow when there is a difference in thermodynamic potential between producers and consumers. Thus, the system operates by balancing energy flows rather than supplying consumers independently [2]. This results in the core governing equation of the model:

$$\sum_i P_i(t) + \sum_i \dot{E}_i(t) = 0; \forall t \in [0, 8760 \text{ h}], \quad (1)$$

where P represents the electrical power supplied by producers, and \dot{E} accounts for energy flows related to consumption and prosumption, having positive or negative sign for energy production and consumption respectively. Index i presents individual energy entities. The basic operation of the modeled system is graphically depicted in Fig. 1.

Corresponding author: Mihael Boštjan Končar

Mihael Boštjan Končar, Domen Hojkar, Boštjan Drobnič, Mihael Sekavčnik and Mitja Mori are with the University of Ljubljana, Faculty of Mechanical Engineering, Ljubljana, Slovenia
(emails: MihaelBostjan.Koncar@fs.uni-lj.si, Domen.Hojkar@fs.uni-lj.si, Boštjan.Drobnic@fs.uni-lj.si, Mihael.Sekavcnik@fs.uni-lj.si, Mitja.Mori@fs.uni-lj.si)

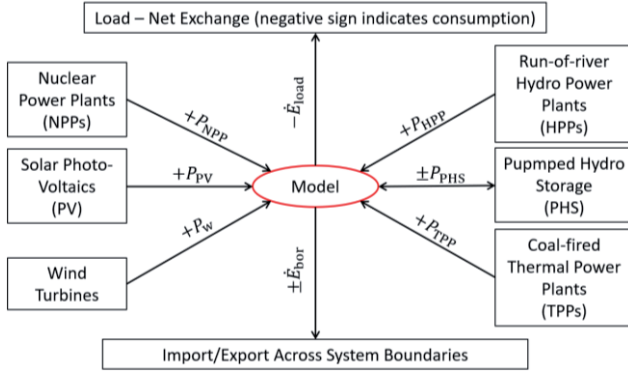


Figure 1. Basic operation of the modeled system

A. ENERGY FLOW MODELING AND SYSTEM DISCRETIZATION

Fig. 1. Basic operation of the modeled system hourly resolution based on the available input data [3]. It should be noted that the approach remains adaptable to finer timescales, provided suitable input data resolution.

Each energy supply technology is modeled according to its characteristics, while consumer demand serves as a boundary condition and was adopted from the grid operator database [3]. Power plants and storage facilities are represented using zero-dimensional models, focusing on integral energy balances. These models leverage empirical correlations or black-box approaches, prioritizing computational efficiency over local process resolution. Such an approach is ideal for system-level studies where energy flow analysis and interactions between system components are paramount. The model is implemented in Python software environment.

B. MODELING DISPATCHABLE AND NON-DISPATCHABLE POWER PLANTS

Nuclear Power Plants

Nuclear power plants (NPPs) typically operate in baseload mode, maximizing power output within the constraints of their fuel cycle. Although modern NPPs allow load-following operation, economic considerations favor continuous operation at rated power [4]. Consequently, the model assumes constant nuclear power generation:

$$P_{NPP}(t) = \text{const.} \quad (2)$$

It is important to note that next-generation nuclear reactors, including Small Modular Reactors (SMRs) and Advanced Micro Reactors (AMRs), demonstrate enhanced load-following capabilities, which are comparable to those of conventional fossil-fueled thermal power plants [4]. Accordingly, the model should be refined to accurately represent these advanced operational characteristics.

Wind and Solar Power Plants

Under Slovenian and European regulations, renewable sources such as wind and photovoltaic (PV) power plants receive priority dispatch [5]. Their power output is determined by the available resource potential:

$$P_w(t) = P_{w, \text{pot}}(t), P_{PV}(t) = P_{PV, \text{pot}}(t). \quad (3)$$

Consequently, these sources inject their entire available power (potential) into the system, irrespective of real-time demand-supply balance.

Hydropower Plants

Run-of-river hydropower plants (HPPs) provide flexible generation, rapidly adjusting their output to stabilize grid frequency and balance stochastic renewable fluctuations. Their power output is modeled using the fundamental hydraulic power equation:

$$P_{HPP} = \eta_{HPP} \rho_{H_2O} \dot{V}_r H_r g, \quad (4)$$

where ρ_{H_2O} is water density, g is gravitational acceleration, \dot{V}_r is volumetric flow rate, H_r is the available hydraulic head, and η_{HPP} is the plant efficiency. Due to computational constraints, actual power potential of modeled HPP is determined using empirical data from a reference hydropower plant (HPP Arto-Blanca), employing a cubic regression model:

$$\hat{P}_{HPP} = C_1 \hat{V}_r \hat{H}_r + C_2 \hat{V}_r^2 \hat{H}_r^2 + C_3 \hat{V}_r^3 \hat{H}_r^3 + C_4 \hat{V}_r \hat{H}_r^3 + C_5 \hat{V}_r^3 \hat{H}_r, \quad (5)$$

where \hat{P}_{HPP} is normalised HPP electrical power, \hat{V}_r normalized volumetric flow rate, \hat{H}_r normalised hydraulic head and C_1 to C_5 are empirical model parameters. The quantities are normalized based on the modeled HPP nominal parameters.

The operation of run-of-river hydropower plants (HPPs) is modeled as a dispatchable source without storage, which represents a deviation from real-world conditions where such dams offer limited storage capacity [6]. In practice, run-of-river dams can provide hourly to daily energy storage; however, within the Slovenian energy system, this capacity is relatively small, typically allowing for only a few hours of storage. Given this constraint, storage effects were considered negligible and thus omitted from the model.

The power output from the HPPs was therefore determined based on instantaneous power potential and system demand. This approach ensures that HPPs do not inject power into the system when demand is absent, effectively simulating the diversion of excess river flow through overflow gates. The HPP model also imposes a minimum operational power limit of 40 % of nominal capacity, meaning that if the current power potential is lower HPP remains offline.

Thermal Power Plants

Coal-fired thermal power plants (TPPs) provide a significant portion of Slovenia's electricity. Their operation follows a trapezoidal generation profile, adjusting gradually to match demand variations. Technical operational constraints include: nominal rated power (typically for SLO ~542 MW_e) ramp rate (typically for SLO ~10 MW_e/min), operating range (typically for SLO ~42%–110% of rated nominal power). Although the technical constraints are well known, the real load variation of TPPs are primarily dictated by energy prices and contractual agreements rather than solely by fuel availability and technical constraints [7]. As economic factors significantly influence dispatch, predicting actual generation without them is not possible. Therefore, the model employs the time-dependent TPP generation profile

based on the typical operation of the Slovenian power system, scaled by a factor k_{TE} , which defines the contribution of TPPs to total power generation:

$$P_{TPP}(t) = k_{TPP} P_{TPP,SLO}(t), \quad (6)$$

where $P_{TPP,SLO}(t)$ represents the data obtained from grid operator.

Gas Turbines

Gas turbines, operating on sub-hourly timescales, are unsuitable for the model's resolution and were thus included in imported energy flows.

C. ENERGY STORAGE MODELING

Slovenia's energy storage infrastructure comprises battery storage systems and Pumped Hydro Storage (PHS). While battery storage operates on sub-hourly timescales, making it unsuitable for this study, PHS provides bulk energy storage with high round-trip efficiency (~78%) [6].

The PHS model is based on the only PHS in Slovenia, PHS Avče [8] and incorporates several simplifications:

- i. in pumping mode PHS operates only at nominal power;
- ii. efficiency of individual system components, excluding turbomachine internal efficiency, remains constant;
- iii. in turbine mode PHS operates between 30% to 100% of nominal power;
- iv. head level variations due to reservoir depletion are neglected;
- v. internal turbine efficiency is interpolated from empirical data for reference Francis turbine.

A detailed description of the PHS model is beyond the scope of this paper; however, its key characteristics are summarized as follows:

- the model incorporates a finite storage capacity that is charged and discharged during PHS operation;
- pumping efficiency is assumed constant, while turbine mode accounts for efficiency variations based on flow conditions and turbomachine characteristics;
- pumping operation is initiated only when excess energy flow in the system meets or exceeds the nominal pump power, at which point it operates at a constant nominal power.

D. SYSTEM ENERGY BALANCE

The energy balance of the system is constructed in multiple steps, incorporating different power generation and storage components to ensure proper alignment of energy supply and demand at each time step. The steps flow:

- i. Energy balance after priority dispatch power plants:

$$\Delta \dot{E}_{sys,1} = P_{prod} - \dot{E}_{load} = P_{JE} + P_w + P_{PV} - \dot{E}_{Load} \quad (7)$$

This step accounts for nuclear power and renewable sources (wind and solar) with priority dispatch.

- ii. Energy balance after including thermal power plants:

$$\Delta \dot{E}_{sys,2} = \Delta \dot{E}_{sys,1} + P_{TPP}(t) \quad (8)$$

This incorporates the contribution of dispatchable coal-fired thermal power plants, which adjust generation according to demand and economic constraints.

- iii. Energy balance after including hydropower plants:

$$\Delta \dot{E}_{sys,3} = \begin{cases} \Delta \dot{E}_{sys,2} + P_{HPP,pot}; & \text{if demand exceeds potential} \\ 0; & \text{if surplus power in system} \\ \Delta \dot{E}_{sys,2}; & \text{if partial HPP load is required} \end{cases} \quad (9)$$

This step introduces run-of-river hydropower generation, balancing residual loads.

- iv. Final energy balance after including pumped hydro storage:

$$\Delta \dot{E}_{bor}^t = \Delta \dot{E}_{sys,4}^t = \Delta \dot{E}_{sys,3}^t + P_{PHS}^t(\Delta \dot{E}_{sys,3}^t, E_{stored}^{t-1}), \quad (10)$$

where P_{HPP} denotes the modeled PHS power, which can be positive (generation) or negative (consumption), depending on the system energy balance $\Delta \dot{E}_{sys,3}$ and the reservoir energy state E_{stored} at the previous time step $t - 1$.

This includes PHS operation. The final energy flow balance $\Delta \dot{E}_{bor}$ defines the required exchange of energy across system boundaries at given time step t , representing imports and exports.

III. BOUNDARY CONDITIONS

The modeled energy system is based on the current state of the Slovenian power system and selected development projections from the National Energy and Climate Plan (NEPN) [1]. Projections for 2040 were analyzed under two scenarios: Renewable and Nuclear Scenario (RS and NS).

The NPP size is based on Krško NPP expansion plans. According to [9] 1200–1600 MWe PWR is optimal for grid stability, with the model assuming a 1200 MWe in NS. Continued operation of the existing unit (696 MWe) is also foreseen in the model for both scenarios.

The boundary conditions for modeled TPPs assume an installed capacity of 542 Mwe ($k_{TPP} = 0.745$) for both scenarios, reflecting TPP Šoštanj, Unit 6.

The run-of-river HPP model is based on volumetric river flow \dot{V}_r and hydraulic head H_r . HE Formin [10], Slovenia's largest HPP, was selected as the reference, with a nominal power of 116 MWe. Hourly river flow data were interpolated from 2020 daily measurements at the Drava-Formin hydrological station [11]. Due to unavailable measured values, H_r was assumed to be 29 m, introducing minimal deviation given stable water level regulation in HPPs. The modeled 1276 MWe hydropower capacity (Slovenia's existing HPP system: 1130 MWe) approximates 11 parallel HE Formin units under identical hydrological conditions. While sufficient for this study, detailed analyses would require individual boundary conditions for each HPP. The same HPP capacity is assumed for both scenarios as foreseen in [1].

Two PHS units were modeled within the system, aligning with projections in [1].

The energy potential of wind and solar power was modeled using meteorological data, with a single reference location selected for each. This simplification deviates from reality, as large-scale deployment at a single site is impossible, due to low energy density. Furthermore, conditions significantly vary by location. However, the reference sites were chosen for optimal wind and solar potential in Slovenia, inherently favoring renewable energy sources.

Wind speed data were obtained from the ARSO automatic meteorological station database [11] for Škocjan na Krasu and adjusted to turbine rotor height with exponential wind profile model. The reference wind turbine, Enercon 66/18.70 [12], was used with its technical characteristics to calculate the actual wind energy potential $P_{w,pot}$. The model assumes 81 wind turbines (installed power 146 MW_e) in NS and 293 turbines in RS (527.4 MW_e), aligning with [1].

Similarly, solar power potential $P_{pv,pot}$ was calculated using 2020 surface solarization data for Koper [13]. The model assumes 3.6 million panels (1,602 MWe) in the NS scenario, reflecting current installed capacity in Slovenia, and 18 million panels (8 GW_e) in the RS scenario, as projected in [1].

Hourly consumption data were obtained from the Slovenian grid operator's database [3], with 2020 as the reference year. Consumption was then scaled by 1.525 to align with the 2040 energy consumption projection [1].

IV. RESULTS

A full discussion of simulation results is beyond this paper's scope; however, key results are outlined in Table 1.

Table 1. Results of the simulation for NS and RS

	NS	RS
share of RES in mix [%]	14	59
imported energy (neg. sign) [TWh]	-0.11	-1.91
exported energy [TWh]	3.19	6.94
net balance [TWh]	3.08	5.03
standard deviation of $\Delta\dot{E}_{bor}(t)$ [kW]	420	1580
carbon intensity of energy mix [kgCO ₂ eq/MWh]	113	148

Across both scenarios, NPPs provided stable baseload generation, minimizing surplus energy while covering most demand. In contrast, wind and solar introduced large surpluses exceeding several GW_e (Fig. 2), requiring storage or substantial exports for system balance. TPPs operated at three discrete power levels (~0%, 40%, 100%), contributing to stability but responding slowly to demand changes due to thermal inertia, leading to minor but predictable surpluses.

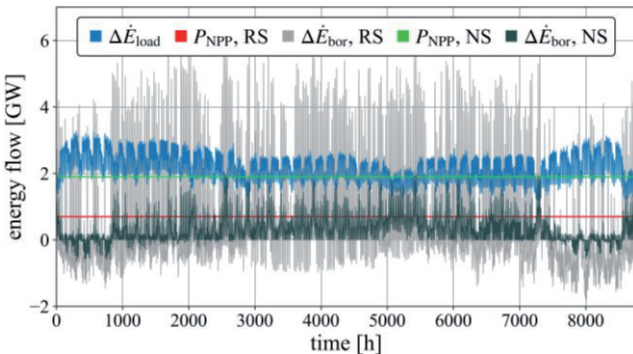


Figure 2. Basic operation of the modeled system

HPPs improved grid flexibility but lacked sufficient storage capacity to mitigate long-term variability. PHS helped stabilize high-power fluctuations but faced charging constraints, limiting its ability to absorb large renewable surpluses (>1 GW_e). Even additional PHS capacity did not significantly improve storage due to the same limitations. Table 1 quantifies fluctuation size through the standard deviation of the final energy balance $\Delta\dot{E}_{bor}(t)$. The carbon intensity of energy mixes was calculated using data from Life Cycle Assessment studies summarized in [14]. Imported energy flows were assigned a footprint of 522 kgCO₂eq/MWh, based on gas turbine emissions [14]. This assumption is justified, as gas turbines are the most likely source of backup generation in interconnected energy markets even outside Slovenia borders [1]. To further assess NPPs' role in decarbonization, an NS variant excluding solar was simulated. In this case, annual imports increased to 0.30 TWh, while exports fell to 1.34 TWh (net balance 1.03 TWh), and carbon intensity increased slightly to 125.6 kgCO₂eq/MWh, demonstrating that a single conventional NPP can replace 8 GW_e of solar capacity, ensuring grid stability with minimal fluctuations while reducing reliance on backup plants, storage, and grid reinforcements, ultimately lowering energy costs while maintaining low emissions.

The environmental impact difference between scenarios is particularly evident in land use requirements: NS requires 2.4 km²/TWh, while RS requires 9.1 km²/TWh. The area was calculated based on [15]. This raises concerns about encroachment on protected areas (e.g., Natura 2000) [1], [15], with potential threats to biodiversity and ecosystem functions, including natural carbon capture capacity.

V. CONCLUSIONS

The analysis demonstrated that nuclear power ensures stable baseload generation, minimizing grid fluctuations and reducing reliance on extensive storage or exports. In contrast, high variable renewables introduced large surplus fluctuations (>1 GW_e), requiring costly balancing measures. Despite similar net energy balances, the nuclear scenario exhibited lower carbon intensity (113 vs. 148 kgCO₂eq/MWh) and almost 4-time lower land use, reducing pressure on ecosystems and biodiversity. A nuclear-only scenario, without solar, achieved carbon intensity of 125.6 kgCO₂eq/MWh, while maintaining a comparable import dependency to that of the NS, highlighting nuclear's undisputable role in decarbonizing energy supply and raising concerns about the feasibility and justification of renewable-only energy policies.

VI. REFERENCES

- [1] Government of the Republic of Slovenia, "Posodobljeni celoviti nacionalni energetske in podnebni načrt Republike Slovenije (NEPN)," Dec. 2024.
- [2] F. Gubina, Delovanje elektroenergetskega sistema. Ljubljana: Fakulteta za elektrotehniko UL, 2006.
- [3] ELES, "Prezem in Proizvodnja," <https://www.eles.si/prevzem-in-proizvodnja>.
- [4] G. Locatelli and others, "Load following with Small Modular Reactors (SMR): A real options analysis," Energy, vol. 80, pp. 41–54, Feb. 2015.
- [5] Zakon o uvajanju naprav za proizvodnjo električne energije iz obnovljivih virov energije (ZUNPEOVE). 2021.

- [6] H. J. Wagner and J. Mathur, *Introduction to Hydro Energy Systems: Basics, Technology and Operation*. London: Springer, 2011.
- [7] K. Strauß, *Kraftwerkstechnik*, 6th ed. Springer, 2009.
- [8] SENG, “Črpalna hidroelektrarna Avče: Od ideje do izvedbe,” Nova Gorica, 2012.
- [9] A. Momirovski and others, “The Impact of JEK2 on the Operation of the Slovenian Electrical Power System,” in *Proceedings of the 30. Conference Nuclear Energy for New Europe 2021, Bled: NSS, Sep. 2021*, pp. 504.1-504.9.
- [10] DEM, “Hidroelektrarna Formin,” <https://www.dem.si/sl/elektrarne-in-proizvodnja/elektrarne/?id=2019090508583024>.
- [11] ARSO, “ARHIV - meteorološki podatki,” <https://meteo.arso.gov.si/met/sl/archive/>.
- [12] Wind-Turbine-Models, “Enercon E-66/18.70,” <https://en.wind-turbine-models.com/turbines/135-enercon-e-66-18.70>.
- [13] JRC-Europe, “Photovoltaic Geographical Information System,” https://re.jrc.ec.europa.eu/pvg_tools/en/#DR.
- [14] M. B. Končar, “Modeling of severe accidents in sodium-cooled fast nuclear reactors,” Master Thesis, University of Ljubljana, Faculty of Mechanical Engineering, Ljubljana, 2023.
- [15] J. K. Noland and others, “Spatial energy density of large-scale electricity generation from power sources worldwi

